Reactive flow and homogenization in anisotropic media

Roded, R., Aharonov, E., Holtzman, R. & Szymczak, P.

Water Resources Research

Key Points:
- Uniform dissolution homogenizes heterogeneous and anisotropic medium and its flow field
- Homogenization is enhanced when the reaction is transport controlled at the pore scale, due to selective dissolution of constrictions
- Under transport-controlled reaction, permeability increase is initially steep but later slows down due to a decrease in reaction rate

Supporting Information:
- Supporting Information S1
- Figure S1

Correspondence to:
R. Roded and P. Szymczak,
roi.roded@mail.huji.ac.il;
piotr.szymczak@fuw.edu.pl

Reactive Flow and Homogenization in Anisotropic Media

R. Roded[1] (ID)**, E. Aharonov[2]** (ID)**, R. Holtzman[3]** (ID)**, and P. Szymczak[4]** (ID)

[1]Hydrology and Water Resources, The Hebrew University, Jerusalem, Israel, [2]Institute of Earth Sciences, The Hebrew University, Jerusalem, Israel, [3]Fluid and Complex Systems Research Centre, Coventry University, Coventry, UK, [4]Institute of Theoretical Physics, Faculty of Physics, University of Warsaw, Warsaw, Poland

Abstract The evolution of heterogeneous and anisotropic media in the uniform dissolution regime (low Damköhler number) is studied here using a numerical network model. The uniform dissolution extensively homogenizes the medium and therefore the flow field. The homogenization is further enhanced when the surface reaction is transport controlled—when slow diffusion of dissolved ions away from the mineral surface leads to the reduction of the global dissolution rate. Under those conditions, diffusive transport is more effective in narrow channels, which selectively enlarge, leading to an initial steep rise of the permeability. However, as dissolution proceeds, the void space widens and the overall dissolution rate drops, and permeability enhancement slows down. Finally, we review the relevance of these results to various processes in geological systems ranging from diagenesis and karst evolution, to carbon geosequestration. These findings provide fundamental insights into reactive transport processes in fractured and porous media and evolution of permeability, tortuosity, anisotropy, and bulk reaction rates in geological systems.

Plain Language Summary When corrosive fluids flow in an aquifer, they dissolve the rocks and change the void-space structure (e.g., acidic water invading limestone). In many geological processes and applications, the flow velocity is high compared to the chemical dissolution rate, and the corrosive fluid penetrates large distances before it loses its reactivity, resulting in relatively uniform dissolution everywhere. Here, using analog numerical model, we study how the void-space structure of porous rocks and aquifers change during uniform dissolution. In particular, we study how different initial structures and reaction conditions change the flow field and transport properties. Finally, we review the relevance of these results to various geological systems. The study improves our understanding of rock and aquifer evolution, with implications to groundwater management and other subsurface flow-related processes, such as CO_2 geosequestration.

1. Introduction

Dissolution induced by reactive flow is a fundamental process in earth systems, controlling the transformation of the medium structure, from the surface (Ford & Williams, 2013) down to the mantle (Aharonov et al., 1995, 1997). It plays a pivotal role in natural processes such as rock weathering, diagenesis, metamorphism, as well as in a wide range of engineering applications (e.g., Lichtner et al., 2018; Steefel & Maher, 2009). Particularly, dissolution controls the evolution of porosity and connectivity in rocks and sediments—a key effect in any application involving subsurface flow, such as groundwater hydrology (Ford & Williams, 2013; Pinder & Celia, 2006), geothermal energy (Huenges & Ledru, 2011), CO_2 geosequestration (Nordbotten & Celia, 2011; Orr, 2009), and hydrocarbon recovery (Agar & Geiger, 2015; Lucia, 2007).

Transport and reaction can be spatially distributed in a different manner. These inhomogeneities can be further amplified by dissolution leading to the emergence of distinct patterns. The dynamic process and the resulting patterns depend on the interplay between advection, diffusion, and reaction, which can be characterized by a pair of dimensionless numbers: (i) the Damköhler number, Da_L, describing the relative rate of reaction versus advection over the length of the system (L) and defined as $Da_L = S\lambda^{eff}L/\overline{v}$, where S is the specific surface area (L^{-1}), λ^{eff} is the effective reaction rate coefficient ($L\,T^{-1}$), and $\overline{v}$ is Darcy flux (or average superficial velocity) and (ii) Péclet number, Pe_L, the relative magnitude of advective and diffusive transport, defined as $Pe_L = \overline{v}L/D$, where D is the diffusion coefficient. Equivalently, their product, $Pe_L Da_L$, is often used instead of Da_L (reaction vs. diffusion, termed Peclet-Damkohler or kinetic number) (Bekri et al., 1995; Golfier et al., 2002; Spiegelman et al., 2001; Steefel & Maher, 2009; Szymczak & Ladd, 2009).

In cases where advective transport is faster than diffusive transport, namely, large Pe_L, dissolution can be either homogeneous or heterogeneous, depending on Da_L. If the reaction rate is high relative to the advection rate across the system (large Da_L), dissolution is enhanced in the most conductive flow paths. This leads to the emergence of reactive-infiltration instabilities and dissolution channels (wormholes), which dramatically increase medium heterogeneity. At lower Da_L, the reactant penetration length, $l_p = L/Da_L$, is very large and the reactive fluid transverses the whole system before its reactivity is exhausted, leading to more homogeneous dissolution, usually referred to as *the uniform dissolution regime* (Golfier et al., 2002; Hoefner & Fogler, 1988; Szymczak & Ladd, 2009). These dissolution regimes are also scale dependent: Instability will develop downstream if the system length, L, is large enough, whereas otherwise homogeneous system dissolution is observed (Starchenko & Ladd, 2018; Steefel & Lasaga, 1990).

While the emergence of instabilities and wormholing development has been studied extensively (Aharonov et al., 1995; Daccord & Lenormand, 1987; Kelemen et al., 1995; Szymczak & Ladd, 2006; Upadhyay et al., 2015), much less attention has been given to the uniform dissolution regime, despite its relevance in many processes, like CO_2 geosequestration (Deng, Steefel, et al., 2018; Gouze et al., 2003; Zhang & DePaolo, 2017), acidizing of sandstone reservoirs (Daccord et al., 1993; Liu & Mostaghimi, 2017; Shafiq & Mahmud, 2017), diagenetic alterations (Taylor et al., 2010; Wray & Sauro, 2017), and karst evolution (Howard & Groves, 1995; Kaufmann & Braun, 1999; Palmer, 2011). Furthermore, even at relatively low flow rates and for large length scales, many geochemical dissolution reactions (e.g., of feldspar minerals or dolomite) are sufficiently slow and expected to produce uniform dissolution (Busenberg & Plummer, 1982; Morse & Arvidson, 2002; Zhu, 2005).

Geological media are commonly characterized by complicated void-space structure, with pore sizes or apertures often spanning several length scales (Blunt, 2017; Palmer, 1991; Sahimi, 2011) and frequently also exhibiting preferred orientation (anisotropy). Specifically, fractured media are associated with anisotropic geometry at different scales—from the surface texture of single fractures (e.g., Aydan et al., 1996; Boutt et al., 2007; Brown & Scholz, 1985; Tatone & Grasselli, 2012; Xie et al., 1999) to fracture networks (Adler et al., 2013; Bonnet et al., 2001; Sahimi, 2011). Furthermore, fault zones that comprise major preferential pathways for reactive fluids (Audra & Palmer, 2015; Klimchouk, 2017) are characterized by highly anisotropic damage zone and directional shearing texture (Candela et al., 2012; Lee & Bruhn, 1996; Renard et al., 2006), as well as anisotropic breccias in fault cores (Bense et al., 2013; Blenkinsop et al., 2007).

Pore-scale anisotropy also exists in permeable rocks (Baas et al., 2007; Benson et al., 2005; Clavaud et al., 2008; Mostaghimi et al., 2013, and references therein), in some cases very pronounced (e.g., Gueguen & Schubnel, 2003; Wright et al., 2009). In particular, in situ differential stresses can induce large anisotropy in the medium, due to the formation of dilatant microcracks aligned parallel to the maximum compressive stress direction. In addition, pores or fractures aligned oblique to the maximum compressive stress preferentially compact and close, further enhancing the anisotropy (Bruno, 1994; Kang et al., 2018; Min et al., 2004; Mitchell & Faulkner, 2008; Sayers, 1990; Simpson et al., 2001).

Yet the evolution of the complex medium structure during dissolution at low Da_L conditions and the resulting transformations of its macroscopic properties are not well understood. In addition, the implications on bulk reaction rates of dissolution itself, a core issue in fluid-rock interaction studies, are still not well quantified (Li et al., 2007; Steefel & Maher, 2009). Understanding the interplay of dissolution and the evolution of medium properties—the main objective of this paper—will improve our ability to decipher the diagenetic history of a medium, as well as to improve subsurface flow applications like groundwater management, intimately linked to the evolved void-space structure.

Of particular interest is the effect of different reaction regimes. Homogeneous dissolution at the system scale is defined to be limited by reaction (as opposed to transport-limited dissolution at higher Da_L conditions; Bekri et al., 1995; Golfier et al., 2002; Varloteaux et al., 2013). However, at the pore-scale dissolution rate can still be limited by transport under some conditions: If the rate of dissolved ion diffusion away from the mineral surface to the bulk fluid is slow (see Figure 1b), transport sustains only limited undersaturation and reactivity adjacent to the surface, and the reaction rate is set by the pore-scale transport rather than by kinetics (here referred as transport-controlled reaction). In such conditions, the characteristic time scale is given by $t_d = r/h$, where r is the void radius and h is the mass transfer coefficient (Golfier et al., 2002;
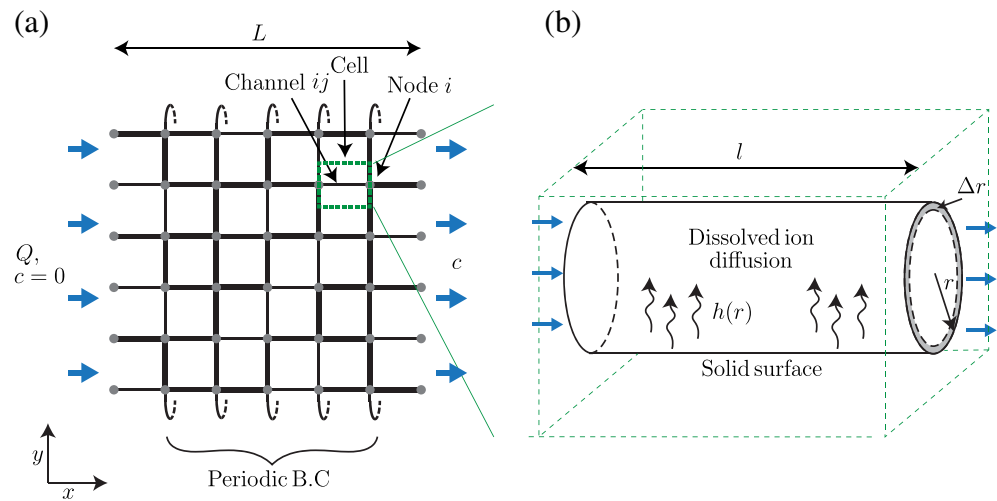
Figure 1. Schematic of the network model of reactive flow and dissolution. (a) The model comprises a square of length L of 2-D regular network of cylindrical channels and nodes (junctions) in a soluble solid. Node i is connected to its neighbor j through channel ij and heterogeneity is introduced via channel sizes. Anisotropy degree, χ (Equation 21), is modified by changing the average size of transverse channels (aligned in the y direction), while the average size of longitudinal channels (aligned in the main flow direction, x) is kept constant. Undersaturated (reactive) fluid, $c = 0$, of constant flow rate, Q, flows from the network inlet face to the outlet face, whereas at the side walls periodic boundary conditions are set. (b) The basic model unit ("cell") includes the channel and the associated solid volume (green frame). The channels are of length l and radius, r which changes by Δr following dissolution over time step Δt. The diffusive mass transfer of dissolved ions to the bulk sustains undersaturation at the mineral surface. Its magnitude is characterized by the mass transfer coefficient $h(r)$.

Gupta & Balakotaiah, 2001; Hanna & Rajaram, 1998; Li et al., 2008). In contrast, if the kinetic rate is slower or the void space is narrow, diffusion is capable of sustaining large undersaturation adjacent to the surface, and the reaction rate is predominantly set by the reaction kinetics (referred here as surface-controlled reaction). In this case, the characteristic time scale is given by $t_r = r/\lambda$, where λ is the reaction rate coefficient (Hoefner & Fogler, 1988; Szymczak & Ladd, 2009).

In this paper, we use a network model to study the dissolution of porous and fractured media at low Da_L. We examine the effect of variable initial medium anisotropy and different reaction regimes. It is shown here that the evolving void-space structure, flow field, and macroscopic properties, as permeability, anisotropy, and reaction rates, are largely controlled by those conditions. The results illuminate the nature of the uniform dissolution regime, which leads to a homogenization of the medium and the flow field.

2. The Network Model

2.1. Network Modeling

To gain a fundamental understanding of dissolution dynamics, we use a network model, with an idealized representation of the void space as a network of discrete channels (Figure 1). This analog approach is often applied to study reactive transport processes, both at the pore scale to core scale in porous rocks (e.g., Algive et al., 2010; Budek & Szymczak, 2012; Hoefner & Fogler, 1988; Nogues et al., 2013; Raoof et al., 2012; Wang et al., 2016; Xiong et al., 2016), as well as at the field scale, in studying karst systems evolution in fractured media (e.g., Dreybrodt et al., 2005; Howard & Groves, 1995; Perne et al., 2014; Rehrl et al., 2008; Skoglund et al., 2010). The explicit but simplified representation of void space in network models allows studying the basic effect of heterogeneity and anisotropy of the medium (Friedman & Jones, 2001; Jang et al., 2011; Steefel et al., 2013; Xiong et al., 2016), while their computational efficiency enables the use of large and representative domains and repetition over multiple realizations. This is in contrast to more accurate methods, such as direct numerical simulations, that are much more restricted by their computational demand (Liu & Mostaghimi, 2017; Molins, 2015; Pereira Nunes et al., 2016).

Despite their simplicity, previous studies demonstrate that regular 2-D and 3-D pore network models can capture well the major characteristics of wormholing observed experimentally, including their structure and advancement rate, and permeability evolution including the breakthrough curve (Budek & Szymczak, 2012; Fredd & Fogler, 1998; Hoefner & Fogler, 1988; Tansey & Balhoff, 2016; Wang et al., 2016). Yet a quantitative agreement can only be expected if the pore network model is constructed based on the real pore structure (Steefel et al., 2013; Xiong et al., 2016). In such a case, the diagenetic history and the porosity-permeability evolution paths of rock samples were successfully reconstructed (De Boever et al., 2012).

Here, we use a 2-D regular network of cylindrical channels embedded in a soluble solid block, a simple representation of a porous media, or a well-connected fractured medium of negligible matrix permeability (Adler et al., 2013; Sahimi, 2011). In particular, the conceptual 2-D network closely resembles the network of permeable channels formed at the intersection of bedding plane with the subvertical fracture network, where karst systems evolution initiate (so-called "inception horizon"; Dreybrodt, 1988; Filipponi et al., 2009; Frumkin et al., 2017).

In the network model, conservation equations for fluid and solute are written for individual pores and nodes (pore junctions). Calculations involve solving the continuity equation for the fluid and Poiseuille's law for the pressure drop in the channels, from which fluid pressures and fluxes are calculated. Solute conservation equations are used to calculate concentrations and mass of solid dissolved. Solute transport in the channels is controlled by advection in the axial direction (flow direction) and by diffusion in the perpendicular (radial) direction, with axial diffusion neglected. This restricts the analysis to conditions where the channel Péclet number is sufficiently large ($Pe_l = \overline{v}l/D \gg 1$, where l is channel length), which are commonly encountered in natural processes and applications (Adler et al., 2013; Ford & Williams, 2013; Niemi et al., 2017), and often lead to uniform dissolution and low Da_L conditions, especially if the reaction is not very fast (Golfier et al., 2002; Niemi et al., 2017; Szymczak & Ladd, 2009). It is noted, however, that mechanical dispersion is inherently incorporated in network models (e.g., Bijeljic & Blunt, 2006).

The large separation of time scales between mineral dissolution and flow and solute concentration relaxation allows to adopt a quasi-static approach (Bekri et al., 1995; Detwiler & Rajaram, 2007; Lichtner, 1991; Sanford & Konikow, 1989). Specifically, the dissolution time scale, corresponding to the time needed for the doubling of the initial pore size (or fracture aperture), is of the order of months to years for the dissolution of carbonates by meteoric waters and up to thousands of years for the dissolution of silicate systems (Dove & Crerar, 1990; Ladd & Szymczak, 2017; Szymczak & Ladd, 2012). The flow and solute concentration relaxation times are several orders of magnitude smaller; thus, the porosity remains essentially frozen on the time scale of momentum and reactant transport, which can then be assumed to be at steady state at each time step. Additionally, as the relaxation time of the flow field is much faster than that of solute, these fields can be calculated sequentially at each time step. The geometrical properties are then updated at the end of each time step to be used in the subsequent step (Ameli et al., 2014; Hoefner & Fogler, 1988; Roded et al., 2018; Szymczak & Ladd, 2009).

2.2. Model Equations and Dimensionless Groups

2.3. Fluid Flow

For an incompressible fluid, the steady-state fluid mass conservation at each node i yields

$$\sum_j q_{ij} = 0, \tag{1}$$

where q_{ij} is the volumetric flow rate through channel ij ($q_{ij} > 0$ indicates flow from node i to j) and the summation is over all neighboring nodes j, linked to node i (Figure 1a and Table 1). The channel flow rates are calculated using Hagen-Poiseuille equation

$$q_{ij} = \frac{\pi r_{ij}^4}{8\mu l}\Delta p_{ij}, \tag{2}$$

where r_{ij} is channel radius, μ is fluid viscosity, and $\Delta p_{ij} = p_i \text{-} p_j$ is the pressure drop between two nodes,

Table 1
Nomenclature

Roman				
A_{cell}	Cell cross section, L^2	U	Amplitude, L
A_{sys}	System cross section, L^2	u	Interstitial velocity, $L\,T^{-1}$
a	Average channel cross section, L^2	V_{cell}	Cell volume, L^3
c	Mixing-cup solute concentration, $M\,L^{-3}$	V_{diss}	Volume of channel dissolved, L^3
c_{eq}	Equilibrium solute concentration, $M\,L^{-3}$	V_f	Volume of fluid injected, T^{-1}
c_{sol}	Concentration of soluble solid, $M\,L^{-3}$	v	Superficial velocity, $L\,T^{-1}$
c_w	Concentration at the wall, $M\,L^{-3}$	$\bar{v}$	Average superficial velocity (Darcy flux), $L\,T^{-1}$
D	Diffusion coefficient, $L^2\,T^{-1}$	x	Coordinate, L
Da_L	Damköhler number	y	Coordinate, L
f	Function	Greek	
G	Transport parameter	γ	Acid capacity number
g	Function	Δ	Difference
h	Mass transfer coefficient, $L\,T^{-1}$	η	Flow focusing parameter
J_r	Reaction rate at the wall, $M\,L^{-2}\,T^{-1}$	λ	Reaction rate coefficient, $L\,T^{-1}$
J_D	Diffusive flux at the channel, $M\,L^{-2}\,T^{-1}$	λ^{eff}	Effective reaction rate coefficient, $L\,T^{-1}$
k	Permeability, L^2	μ	Fluid viscosity, $M\,L^{-1}\,T^{-1}$
L	System length, L	ν	Stoichiometric coefficient
l	Channel length, L	ρ	Coordinate, L
l_{en}	Entrance length, L	ξ	Axial coordinate, L
l_p	Penetration length, L	τ	Tortuosity
N	Number of channels	χ	Anisotropy degree
n_{50}	Fraction of longitudinal channels carrying half of the total flow	χ'	Anisotropy degree after dissolution
Pe_L	System-scale Péclet number	Ω_S	Bulk reaction rate, $mol\,L^{-2}\,T^{-1}$
Pe_l	Channel Péclet number	Ω_{St}	Bulk reaction rate after dissolution, $mol\,L^{-2}\,T^{-1}$
p	Fluid pressure, $M\,L^{-1}\,T^{-2}$	ω	Angular frequency, L^{-1}
Q	Total volumetric flow rate, $L^3\,T^{-1}$	Subscripts	
q	Channel volumetric flow rate, $L^3\,T^{-1}$	W	Wavy channel
$\bar{q}$	Inlet channel average flow rate, $L^3\,T^{-1}$	in	Inlet
r	Channel radius, L	out	outlet
S	Specific surface area, L^{-1}	I	Coordinate index, $I = x$ or y
Sh	Sherwood number	i	Nodes index
s	Channel surface area, L^2	j	Neighboring nodes index
s_T	Total system surface area, L^2	x, y	Channels alignment direction
t	Time, T	0	Initial average quantity
t_d	Characteristic time scale of transport, T	Superscripts	
t_r	Characteristic time scale of reaction, T	$-$	Average quantity
		$\char94$	Scaled quantity

which are a distance of l apart. The system of linear Equations 1 and 2 is solved for pressure values at the nodes.

2.3.1. Reactive Transport and Dissolution

Assuming first-order reaction kinetics, the reaction rate at the channel surface is

$$J_r = \lambda\ c_{eq} - c_w\ , \tag{3}$$

which depends on the difference between the solute concentration at the wall, c_w, and the equilibrium concentration, c_{eq}, and λ is the kinetic reaction rate coefficient (L/T). Reaction products (e.g., calcium ions) then diffuse away from the mineral surface to the bulk fluid and sustain undersaturation conditions at the wall (Dreybrodt et al., 2005; Hanna & Rajaram, 1998). This diffusive flux can be expressed by

$$J_D = h(c_w - c), \tag{4}$$

where c is the flow-weighted average concentration (mixing-cup concentration), defined as $c = \frac{1}{q}\int_0^r c(\rho)u(\rho)2\pi\rho d\rho$, with u the fluid velocity and ρ the radial coordinate. Next, h is the mass transfer coefficient, which is inversely proportional to the radius and calculated using

$$h(r) = \frac{DSh}{2r}, \tag{5}$$

where D is the molecular diffusion coefficient and Sh the Sherwood number (Bejan, 2013; Gupta & Balakotaiah, 2001). Sh depends on λ and is bound by two asymptotic limits that are close to each other in value (the transport and kinetic limits, $Sh = 4.364$ and 3.656, respectively; Gupta & Balakotaiah, 2001; Hayes & Kolaczkowski, 1994). Here Sh is approximated by a constant value, $Sh = 4$ (Budek & Szymczak, 2012; Noiriel & Deng, 2018). This assumption is adequate as long as the solute entrance length, l_{en}, required to reach the asymptotic value is small ($l_{en} \ll l$). The entrance length increases as the radius and fluid velocity increase (see e.g., Bejan, 2013; Rohsenow et al., 1998) but remains small in our numerical simulations.

The reaction rate and the diffusive flux (Equations 3 and 4) are equal at the steady state and can be used to express the concentration at the wall in terms of the average one

$$c_{eq} - c_w = \frac{c_{eq} - c}{1 + \lambda/h(r)}. \tag{6}$$

Next, expressing the reaction rate (Equation 3) in terms of the averaged concentration leads to

$$J_r = \lambda^{eff}\ c_{eq} - c\ , \tag{7}$$

where the effective reaction rate coefficient (Budek & Szymczak, 2012; Noiriel & Deng, 2018), which incorporates both kinetics and transport effects on reaction rate, is

$$\lambda^{eff} = \frac{\lambda}{1 + g(r)}, \tag{8}$$

with the function g, defined as

$$g(r) = \frac{\lambda}{h(r)}. \tag{9}$$

The parameter $g(r)$ is the ratio between the characteristic time scales of transport $t_d = r/h$ and reaction, $t_r = r/\lambda$, and accounts for the extent by which dissolution rate within a single channel is hindered by transport; when $g \ll 1$ reaction rate is surface controlled and limited by kinetics and when $g \gg 1$, the reaction is transport controlled.

Dissolution in the channels is modeled assuming advection-dominant transport along the axial direction, ξ, ($Pe_l \gg 1$), and radial transport effects are incorporated in the effective reaction coefficient, λ^{eff}, resulting in a 1-D advection-reaction equation

$$q\frac{dc}{d\xi} = -2\pi r\lambda^{eff}\ c_{eq} - c\ , \tag{10}$$

Note that in the above, indices associated with individual channels and nodes (cf. Equations 1 and 2) were dropped for clarity of presentation. For a given solute concentration at the channel inlet, $c(\xi = 0) = c_{in}$, Equation 10 can be solved for the concentration at the channel outlet, $c(\xi = l) = c_{out}$

$$c_{out} = c_{eq} -\ c_{eq} - c_{in}\ e^{-s\lambda^{eff}/q}, \tag{11}$$

where $s = 2\pi rl$ is the channel surface area. Lastly, the concentration of solute at the nodes is calculated from channel outlet concentrations, c_{out}, and solute balance, assuming full mixing at the channel intersections.

Given the reaction rate (Equation 7), the erosion rate of the channels can be calculated based on the mass conservation

$$\frac{\partial r}{\partial t} = \frac{\lambda^{eff}}{\nu c_{sol}}\ c_{eq} - c\ , \tag{12}$$

where c_{sol} is the molar concentration of soluble solid material and ν accounts for the stoichiometry of the reaction (Algive et al., 2010; Detwiler & Rajaram, 2007). Then, the total volume of mineral dissolved from a single channel surface during a time step Δt can be calculated using

$$\Delta V_{diss} = \frac{2\pi r \Delta t \lambda^{eff}}{\nu c_{sol}} \int_0^l \left(c_{eq} - c(x) \right) \, \mathrm{d}x = \Delta t \, q \frac{c_{eq} - c_{in}}{\nu c_{sol}} \left(1 - e^{-s\lambda^{eff}/q} \right) . \tag{13}$$

In order to keep the model tractable, we assume that each cylindrical channel dissolves uniformly along its length. The corresponding change in channel radius is then

$$\Delta r = \frac{\Delta V_{diss}}{s} = \frac{\Delta t q}{s} \frac{c_{eq} - c_{in}}{\nu c_{sol}} \left(1 - e^{-s\lambda^{eff}/q} \right) . \tag{14}$$

The model also accounts for a finite amount of soluble solid, and if locally between adjacent channels solid is fully dissolved, channel merging is accounted for by the associated hydraulic conductivity increase (see Roded et al., 2018).

2.3.2. Dimensionless Groups Characterizing Network Evolution

As observed from Equation 11, the decay of undersaturation between channel inlet and outlet (c_{eq}-c_{out}) is determined by a function

$$f(r, q) = \frac{s\lambda/q}{1 + g(r)} = \frac{s\lambda^{eff}}{q}, \tag{15}$$

which comprises the ratio between the reactive and advective transport rates. The relative change in radius can then be expressed in terms of the functions f and g and Equation 14

$$\frac{\Delta r}{r_0} = \frac{\Delta \hat{t} \left(c_{eq} - c_{in} \right)/c_{eq}}{(1+g)f} \left(1 - e^{-f} \right), \tag{16}$$

where r_0 is the initial average channel radius and $\hat{t}$ is the dimensionless time, defined as

$$\hat{t} = \frac{\lambda t \gamma}{r_0}. \tag{17}$$

Here $\gamma = c_{eq}/c_{sol}\nu$ is the acid capacity number, defined as the ratio between the number of molecules in a unit volume of a mineral to the number of molecules of the solute in a unit volume of fully saturated fluid ($c_{in} = 0$ is assumed at the domain inlet). The functions f and g characterize dissolution in channels, with dependence on time arising through r and q. To characterize the effects of transport and reaction rates on the dissolution process, we calculate f and g from the initial averaged parameters of the longitudinal channels, aligned in the main flow direction, x. This leads to the following definition of the dimensionless Damköhler number:

$$Da_L = \frac{s_0 \lambda L}{l \bar{q}(1 + G)} = \frac{S\lambda^{eff} L}{\bar{v}}, \tag{18}$$

and

$$G = \frac{\lambda 2 r_0}{D Sh}, \tag{19}$$

where s_0 and S are the initial average and specific surface area of longitudinal pores and calculated using $s_0 = \Sigma s_x/N_x$ and $S = s_0/V_{cell}$, where subscript x is for longitudinal channels, N is the total number of channels, and V_{cell} is cell volume (comprising the channels and the associated solid volume; see the green frame in Figure 1). Next, $\bar{q}$ and $\bar{v}$ are the average inlet flow rate and superficial velocity and calculated using $\bar{q} = Q/N_{in}$ and $\bar{v} = \bar{q}/A_{cell}$, where N_{in} is the total number of inlet nodes, A_{cell} is cell's cross-sectional area, and $V_{cell}/A_{cell} = l$. Note that the Péclet number does not appear in these equations because the diffusive effects in the axial direction are neglected.

2.4. Simulation Setup

2.4.1. Initial and Boundary Conditions

We consider the inflow of undersaturated fluid of constant total volumetric flow rate, Q, from network inlet face to outlet face and impose the pressure at the boundaries

$$p(x = 0, y) = p_{in} \quad \text{and} \quad p(x = L, y) = 0. \tag{20}$$

As permeability increases in the course of dissolution, to maintain the flow rate, Q, fixed, the pressure at the inlet nodes is adjusted at every time step. Along y (transverse) direction, periodic boundary conditions for flow and transport are set, and concentration at the outlet nodes is calculated from solute mass conservation (Equation 11; free-flow boundary).

2.4.2. Network and Reactive Transport Settings

We use a regular rectangular network of 100×100 nodes and consider heterogeneity in channel volumes by sampling their diameters from a lognormal distribution with a relative standard deviation of 2.25. Such a wide pore size distribution is typical of geological media (Lucia, 2007; Sahimi, 2011). To obtain representative results for the heterogeneous media, the results were averaged using 20 realizations of statistically similar properties.

Anisotropy is implemented by changing the *average* size of transverse channels (perpendicular to the main flow direction, y), whereas the initial *average* size of the longitudinal channels is initially the same in all simulations. Anisotropy degree is defined as

$$\chi = \frac{a_x - a_y}{a_x + a_y}, \tag{21}$$

where a is the average cross section of the cylindrical channels, calculated using $a_I = \Sigma \pi r_I^2 / N_I$, where subscript index I is y or x, denoting transverse and longitudinal channels, respectively. χ is negative for wide transverse channels and positive for narrow ones. In some instances, anisotropy can be very pronounced, for example, in the case of unidirectional tensile joints, with permeability ratio of orders of magnitude between orthogonal directions (Adler et al., 2013; Barton, 2006). Consequently, we study a wide range of anisotropy degree, χ, in between -0.98 and 0.98, corresponding to a ratio of 100 between cross sections of the channels aligned in orthogonal directions.

Each time step begins with calculation of the flow field by solving the system of Equations 1 and 2. Next, using the channel flow rates, q, the solute concentration at the nodes is calculated by solving Equation 11 and solute balance in nodes. Lastly, the change in pore radii is calculated using Equation 14. The time step is small enough so that the changes in pore radii will constitute a small fraction of the original radius. Additionally, a sensitivity test of the effect of time step was performed: Simulations were run with decreasing time step until the volume of reactive fluid (V_f) needed to achieve 100-fold permeability increase stabilized.

We focus here on relatively uniform dissolution, where the reaction rate is low compared to advective transport, setting $Da_L = 0.1$. The Damköhler number is calculated based on the average radius of longitudinal channels, which is initially the same in all the simulations (incorporated in Equation 18 through s and G). To study the effect of different reaction regimes, G is altered (100, 1, and 0.01) by modifying the reaction rate coefficient, λ. In order to maintain Da_L constant while varying λ, the flow rate $\bar{q}$ is changed accordingly (cf. Equations 18 and 19). The Péclet number is kept large in all simulations ($Pe_l > 10^5$) corresponding to the assumption of the dominance of advective transport considered here.

The model was implemented in Matlab computer code (MATLAB, 2018). The simulations were running on PC, with quad intel (R) Core (TM) i7-7700 CPU, 3.600 GHz, and 32 GB RAM, and run time was 10–40 s for a single simulation.

3. Results and Discussion

3.1. Media and Flow Field Homogenization

Prior to dissolution, the flow regime is governed by the imposed initial anisotropy, which controls flow focusing into preferential pathways and flow tortuosity (Jang et al., 2011; Sahimi, 2011; Thompson &
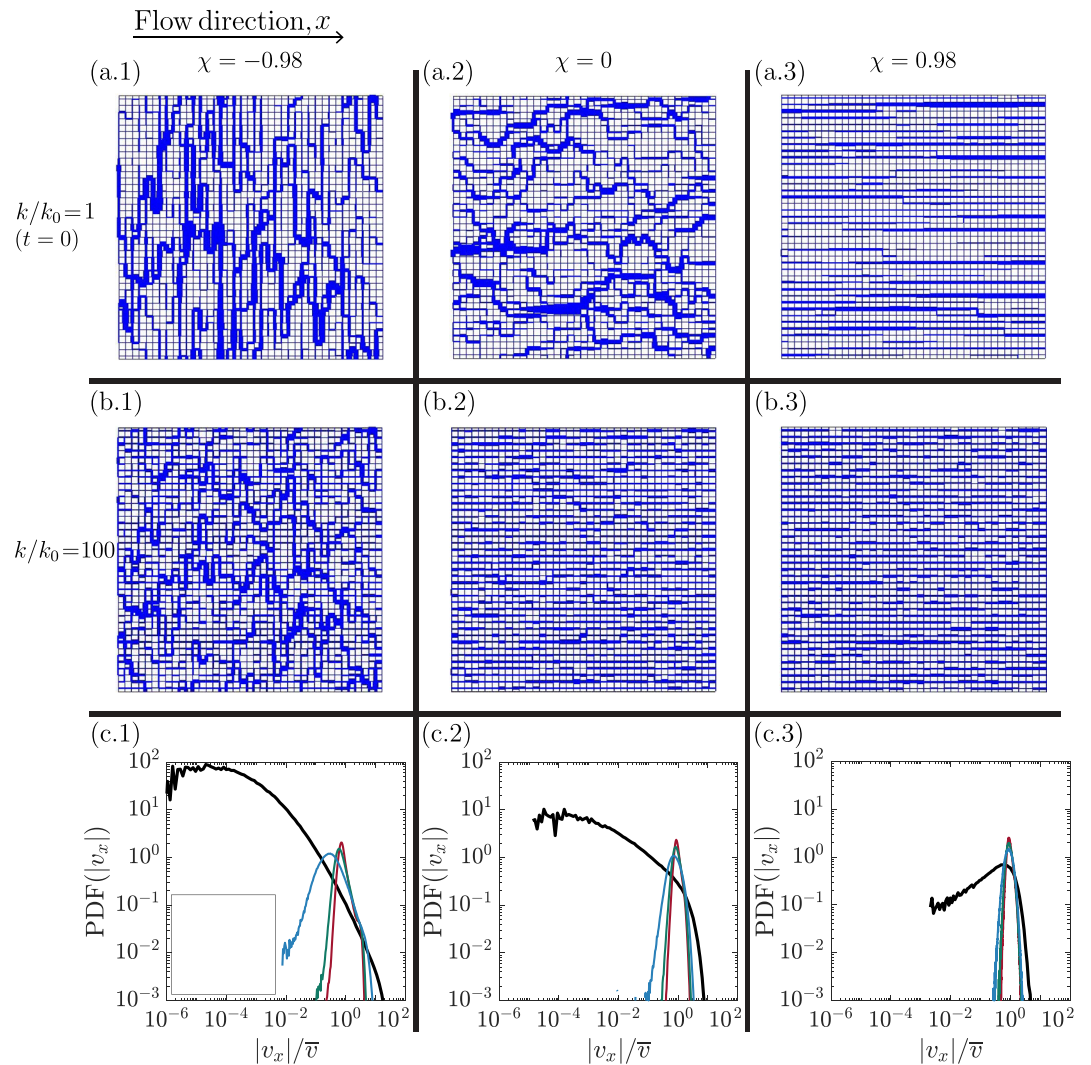
Figure 2. The graphical representation of the flow field in the initial (a) and dissolved system (b) and the corresponding velocity distributions (c). For wider transverse channels aligned perpendicular to flow direction, and lower χ, the flow is more heterogeneous and focused in preferential tortuous pathways (a). Following dissolution, the flow field is extensively homogenized ($G = 1$) (b). These effects are also manifested in the probability density function (PDF) of the velocities, where v_x and $\bar{v}$ are the superficial velocities and their average in longitudinal channels (c). At $t = 0$ (black line) for lower χ, flow is highly heterogeneous with a large number of low velocity values, spanning many orders of magnitude. The change to narrower peaks following dissolution indicates a transition to a more uniform flow field, which is enhanced for large G (see text). In (a) and (b) line widths are proportional to the magnitude of v, normalized by 20th to 80th velocity percentage range of the flow field, v_{80th}-v_{20th}. Panels (b) and (c) are shown after a prescribed volume of reactive fluid has been injected, corresponding to a 100-fold permeability increase in the isotropic system ($\chi = 0$) with respect to its initial value, $k_0(k/k_0 = 100)$, with $G = 1$.

Brown, 1991). This can be seen in Figures 2a.1–2a.3, which show initial flow for networks of different anisotropy. The presence of wide transverse channels ($\chi = -0.98$) promotes bypassing narrow constrictions in the longitudinal direction. In this case, flow focuses in highly conductive tortuous pathways with dominant transverse flow components (Figure 2a.1), resulting in relatively high overall permeability of the medium, k (Figure 3a) (calculated using Darcy's law, $Q = (A_{sys}k/\mu)(p_{in}/L)$, where A_{sys} is the system cross-sectional area, $A_{sys} = N_{in}A_{cell}$).

In contrast, the presence of narrow transverse channels ($\chi = 0.98$) leads to a more direct and relatively uniform flow in the longitudinal direction (Figure 2a.3), which also limits the overall permeability (Figure 3a), because any narrow constrictions along the longitudinal paths are difficult to bypass. Theoretical bounds for
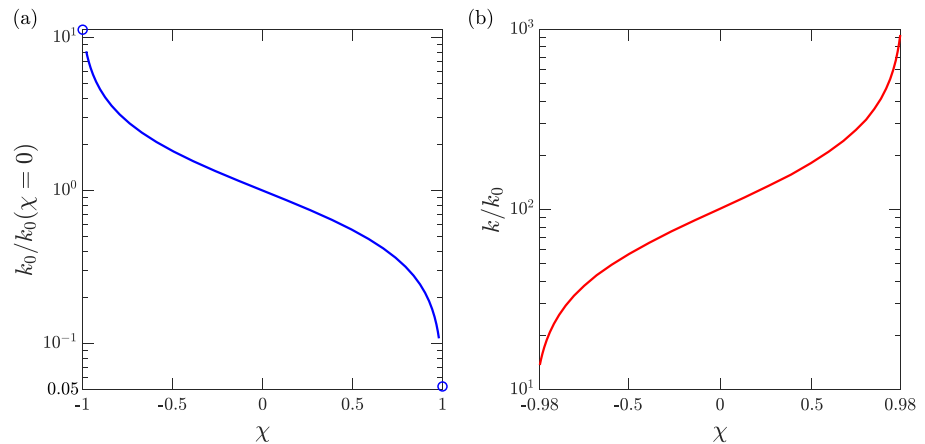
Figure 3. (a) Initial permeability, k_0, of the system as a function of the anisotropy degree, χ. For wide transverse channels and $\chi = -0.98$, initial permeability is higher by almost 2 orders of magnitude compared to the system with narrow transverse channels and $\chi = 0.98$. Circles mark upper and lower bounds for permeability for the limiting cases of transverse channels of infinite width, $\chi \to -1$, and no transverse channels, $\chi = 1$; permeability is normalized by the permeability of the isotropic system, $k_0(\chi = 0)$. (b) The normalized increase in permeability, k/k_0, following dissolution for systems with different χ. The dissolution is stopped after a prescribed volume of reactive fluid has been injected, corresponding to a 100-fold permeability increase of the isotropic system ($\chi = 0$) for $G = 1$. At this point, the permeability in a system with wide transverse channels, $\chi = -0.98$, increases only by ~1 order of magnitude compared to ~3 orders of magnitude for $\chi = 0.98$.

permeability are provided by considering the extreme cases of (i) no transverse channels, $\chi = 1$, and (ii) transverse channels of infinite width, $\chi \to -1$ (blue circles in Figure 3a; Hunt & Ewing, 2009; Jang et al., 2011). The effect of anisotropy on flow is also manifested through the probability density function (PDF) of the velocities (Figure 2c), where v_x is the superficial velocity in the longitudinal channels, calculated using $v_x = q_x/A_{cell}$. Before dissolution takes place (at $t = 0$, black line) for wide transverse channels, $\chi = -0.98$, flow heterogeneity is large with high number of low velocity values, spanning many orders of magnitude. No clear maximum in the distribution can be detected for $\chi = -0.98$ and 0. Conversely, for narrow transverse channels, $\chi = 0.98$, the flow is much more uniform with a well-defined maximum in the distribution.

Following dissolution, velocity distribution and the medium structure become more uniform with a clear maximum appearing in all distributions (Figures 2b and 2c). Both very low and very high velocities disappear from the distributions. The velocity distribution after dissolution depends considerably on the extent by which transport hinders reaction, characterized by the parameter G (Equation 19). When the reaction is surface-controlled (low G), dissolution increases channel sizes uniformly in the medium, homogenizing the transport properties and hence also the flow field. Under transport-controlled reaction conditions (large G), the homogenization process is even further enhanced, due to a more intense dissolution in the narrow channels compared to the slower dissolution in wider conduits (see supporting information Figure S1 for a comparison of the resulting flow field with $G = 0.01$, 1, and 100). For large G, the dissolution rate is mostly controlled by the diffusion rate of dissolved ions from the mineral surface to the bulk fluid, which is faster in narrower conduits (Varloteaux et al., 2013). This effect is manifested in the velocity distribution, with a smaller fraction of lower velocities (corresponding to flow in the narrow channels) at large G, compare Figure 2c.

To further quantify the changes in the flow field, we use two parameters: (i) tortuosity τ and (ii) the degree of flow focusing η. Here τ is defined as (Koponen et al., 1996; Matyka & Koza, 2012)

$$\tau = \frac{\langle |v| \rangle}{\langle v_x \rangle}, \tag{22}$$

which in the orthogonal and regular network can be calculated using $\tau = \Sigma(|v_x| + |v_y|)/\Sigma v_x$, where the summation is performed over all the channels. Flow focusing, $\eta = n_{50}^{-1}$, is evaluated from the fraction
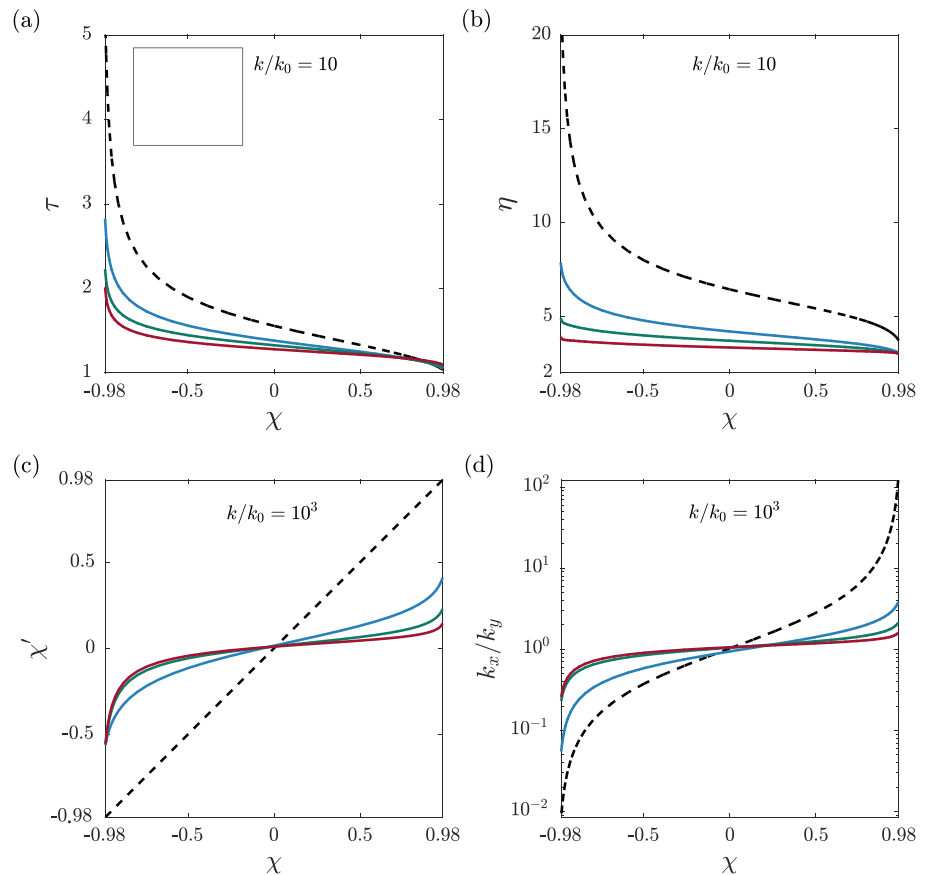
Figure 4. Flow field and media properties as a function of anisotropy degree, χ, before (black dashed line) and after dissolution for different values of the transport parameter G. (a) tortuosity τ, (b) flow focusing parameter, η, (c) anisotropy degree after dissolution, χ', and (d) permeability anisotropy, k_x/k_y (see the text for definitions). Plots show results for dissolved systems after the permeability has increased 10-fold or 1,000-fold from its initial value, that is, $k/k_0 = 10$ or 1,000, as specified in each plot. Dissolution leads to homogenization and τ and η decline more steeply for systems with initially more conductive transverse channels, that is, systems with $\chi < 0$. Dissolution also leads to a more isotropic system, by decreasing differences between the longitudinal and transverse directions. This is seen in both the average size of channels and the permeabilities ($\chi' \to 0$ and $k_x/k_y \to 1$). These effects are enhanced when the reaction is hindered by diffusion, $G = 100$, and $G = 1$, due to intensified growth of the narrow channels.

of longitudinal channels that carry half of the total flow, n_{50} (Jang et al., 2011). The changes in τ and η are especially pronounced when the transverse channels are initially more conductive ($\chi < 0$), and flow is focused and highly tortuous (Figure 2a.1). At those conditions, the initial highly heterogeneous flow field is homogenized by the dissolution in narrow longitudinal channels, which creates flow shortcuts that reduce tortuosity and flow focusing (Figures 2b.1, 4a, and 4b). After extensive dissolution ($k/k_0 = 10^3$; not shown in Figure 4), the flow field is almost perfectly homogenized, with τ and η approaching their minimum values, $\tau = 1$ and $\eta = 2$, corresponding to completely direct and uniform flow, respectively.

The homogenization by the uniform dissolution also acts to decrease system-wise anisotropy, reducing the difference in the sizes of the channels in orthogonal directions (anisotropy degree following dissolution χ' approaches zero, Figure 4c). Similarly, when the reaction is inhibited by transport, $G = 100$ and $G = 1$, the homogenization is enhanced and leads to a more isotropic system, due to intensified growth of the narrow channels. We note the small differences in anisotropy degree following dissolution, χ', between fully and partially hindered reaction, $G = 100$ and $G = 1$. This is due to a competition: For $G = 100$ dissolution effectively acts to reduce anisotropy due to focused dissolution in the narrow channels; however, as the channels widen, strong transport inhibition leads to a decline of reaction rate, which in turn decreases the rate of homogenization compared to $G = 1$, leading eventually to a similar outcome.
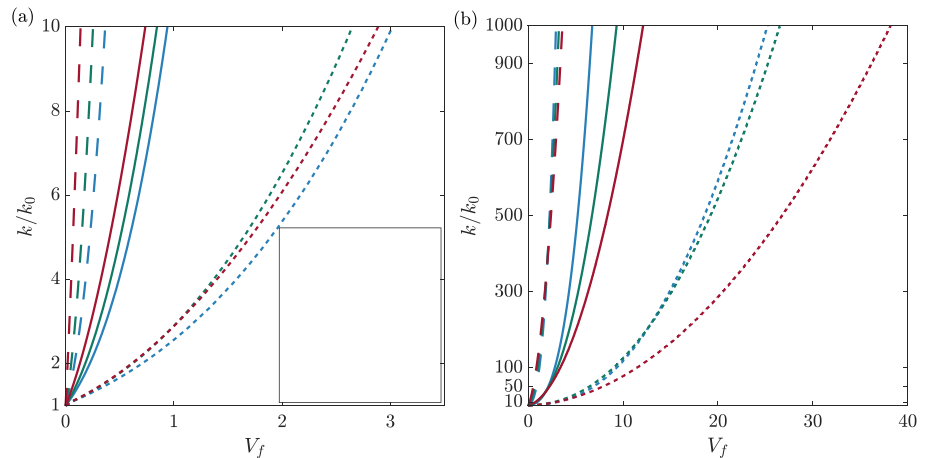
Figure 5. The enhancement of permeability, k/k_0, with the volume of reactive fluid injected, V_f, for different values of anisotropy degree, χ, and transport parameter, G. Panel (a) shows the initial part of the curves, up to $k/k_0 = 10$. For narrow transverse channels, $\chi = 0.98$, and low initial permeability, k_0, permeability increases by orders of magnitude after a relatively small volume of reactive fluid has been injected. Conversely, for wide transverse channels, $\chi = -0.98$, a relatively large amount of reactive fluid is required to produce the same permeability increase. Permeability evolution is also affected by the transport parameter, G: Higher G leads to steeper permeability enhancement at an early stage (a). After further dissolution, this trend flips and permeability enhancement is faster for lower G (b).

The reduction in anisotropy is also evident in the permeability anisotropy following dissolution: As the dissolution progresses, the transverse permeability approaches that in the longitudinal direction, $k_x/k_y \rightarrow 1$ (Figure 4d). Interestingly, also when anisotropy degree, χ, is initially large and the injection is in the direction of the more conductive channels, the system becomes more isotropic and both anisotropy degree, χ, and permeability anisotropy, k_x/k_y, decrease. Another observation is that an initially isotropic system ($\chi \rightarrow 0$) remains so following dissolution.

In the case of 3-D networks, the initial flow field tends to be more heterogeneous and focused in preferential pathways, relative to 2-D (Fiori & Jankovic, 2012). In such a case, it is expected that the homogenization effect and the associated change in properties will be even more intense. That is because the flow field homogenization is more pronounced when the initial flow heterogeneity is large.

3.2. Permeability Evolution

Pronounced effects of anisotropy degree, χ, and transport parameter, G, on network structure and flow field are also manifested in the longitudinal permeability evolution as shown in Figure 5. Here, V_f is defined as the volume of reactive fluid injected, normalized by the system volume. For narrow transverse channels, $\chi = 0.98$, and low initial permeability, relatively small amount of reactive fluid injection, V_f, leads to a steep enhancement of permeability (Figures 3b and 5). In contrast, with wide transverse channels, $\chi = -0.98$, and focused preferential flow, significant reactive fluid injection, V_f, and dissolution are required to attain the same permeability increase.

The effect of the reaction regime on permeability is milder than that of anisotropy, however, more intricate and evolving with time. At the initial stage of dissolution, permeability increases faster with larger G (Figure 5a). This is because at transport-controlled conditions (large G) dissolution primarily takes place at narrow channels that affect the flow considerably and their dissolution leads to steep permeability enhancement. As dissolution proceeds, this trend flips and $k/k_0 = 10^3$ is reached earlier under surface-controlled conditions (low G; Figure 5b). This change is attributed to the steady growth of the channels under the surface-controlled dissolution, and the corresponding slowdown of the growth when the reaction is hindered by transport as the dissolution proceeds.

3.3. Theoretical Results of Simplified System: A Wavy Channel

To analyze and demonstrate further the effect of the transport parameter G, we consider a simplified model system: a single channel with a wavy profile and repeated constrictions and dilations (black line in
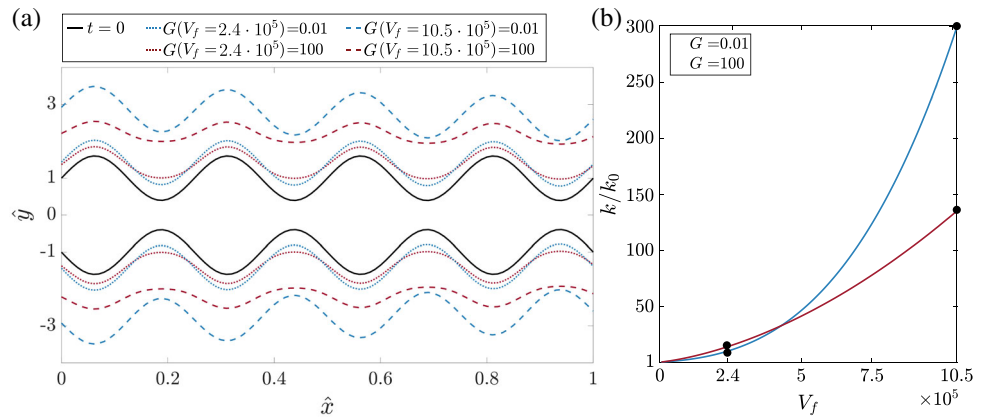
Figure 6. Dissolution of a wavy channel: (a) the channel profile at $t = 0$ (black line) and after a prescribed volume of reactive fluid, V_f, has been injected, for transport-controlled reaction, $G = 100$ (red lines), and surface-controlled reaction, $G = 0.01$ (blue lines). (b) The increase in channel permeability, k, with injected volume, V_f (the black dots are for $V_f = 2.4 \cdot 10^5$ and $10.5 \cdot 10^5$ shown in [a]). While for $G = 100$ dissolution is enhanced in the constrictions, flattening the channel profile, for $G = 0.01$ the channel erodes more uniformly. Permeability increase is steep at an early stage for $G = 100$, due to enhanced dissolution in the constrictions. However, as the channel grows wider, transport limitation becomes substantial and permeability enhancement becomes faster for $G = 0.01$. The coordinates $\hat{x}$ and $\hat{y}$ are scaled with the channel length, L, and initial average radius, r_0, respectively, and V_f is normalized by the initial channel volume; in all cases shown here $Da_W = 0.1$.

Figure 6a). This allows us to calculate the geometry evolution analytically and numerically (details of these methods are described in Appendix A). The characteristic dimensionless numbers for the channel are $Da_W = \dfrac{2\pi r_0 L \lambda}{q(1 + G)}$ and G (the latter given by Equation 19).

When the reaction is transport controlled ($G = 100$), dissolution is enhanced at the channel constrictions (Deng, Molins, et al., 2018; Dykaar & Kitanidis, 1996), flattening the channel profile and making it more uniform (red lines in Figure 6a). Conversely, for surface-controlled reaction ($G = 0.01$), the channel erodes more uniformly, preserving the original profile shape (blue lines). The permeability evolves in a similar manner to that in the network model: At an early stage of the dissolution, for large G, channel permeability increase is steep due to enhanced dissolution of the constrictions, which are the main factor limiting the flow (Figure 6b). But as dissolution proceeds and the channel grows wider the transport limitation has an increasing effect, the reaction rate declines, and as a result, permeability enhancement is larger for $G = 0.01$ (see the wider channel for $G = 0.01$ for $V_f = 10.5 \cdot 10^5$ in Figure 6a). The calculation of channel permeability, k, is described in Appendix B.

3.4. Reaction Rate

The macroscopic (bulk) reaction rate depends on the intrinsic (batch) rate and the transport conditions, both at the pore scale and system scale. There is an intricate feedback between the void-space structure, transport, and reaction rate—transport closely depends on the detailed structure, which can evolve during the dissolution process, and consequently, reaction rate also evolves in time. Here, we study the effect of changing the anisotropy degree and the mode of transport, G, on the time-dependent bulk reaction rates.

The reaction rate (mol/L^{2}T) along the channel can be calculated using

$$\Omega(\xi) = \lambda^{eff} \left(c_{eq} - c(\xi) \right) , \tag{23}$$

The average reaction rate along the channel is then

$$\Omega = \frac{1}{l} \lambda^{eff} \int_0^l \left(c_{eq} - c(\xi) \right) \, d\xi, \tag{24}$$

$c(\xi)$ is obtained by solving Equation 10 using $c(\xi = 0) = c_{in}$; this leads to
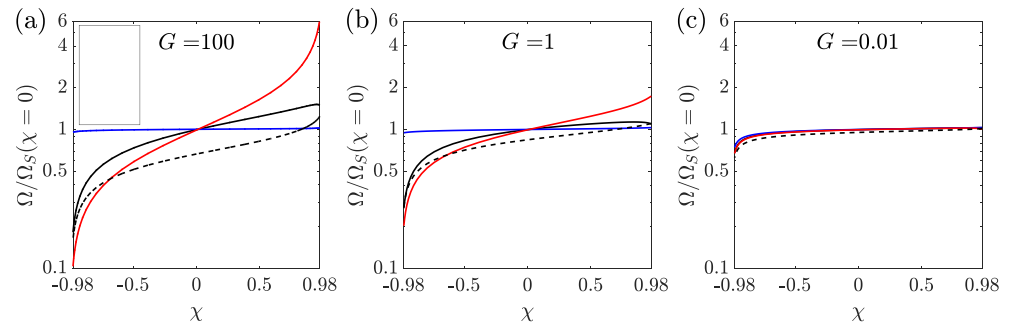
Figure 7. The macroscopic (bulk) reaction rates, Ω_S (mol/L^{2}T), as a function of anisotropy degree, χ, for different values of the transport parameter, $G = 100$, 1, 0.01 (a–c). Ω_{S0}, Ω_{x0}, and Ω_{y0} are the reaction rates at $t = 0$ in the whole system (solid black line), as well as in the longitudinal (blue curve) and transverse channels (red curve), respectively. Ω_{St} is the macroscopic reaction rate following dissolution when $k/k_0 = 10^3$ (dashed black line). Under transport-controlled conditions, $G = 100$, the initial reaction rates, Ω_{S0} and Ω_{y0}, as well as Ω_{St} strongly depend on χ, whereas Ω_{x0} is almost constant. Under surface-controlled reaction conditions, $G = 0.01$, the bulk rates are relatively insensitive to χ. The rates are normalized by the reaction rate of the isotropic system at $t = 0$, $\Omega_{S0}(\chi = 0)$.

$$\Omega = \frac{1}{l}\lambda^{eff}\int_0^l \left(c_{eq} - c_{in}\right) e^{-2\pi r\lambda^{eff}\xi/q}\,\mathrm{d}\xi = q\left(c_{eq} - c_{in}\right)/s\left(1 - e^{-s\lambda^{eff}/q}\right). \tag{25}$$

The bulk reaction rate for the entire system can then be calculated by $\Omega_S = 1/s_T\,\Sigma(s\Omega)$, where s_T is the total geometric surface area in the network and the summation is done over all the channels. To quantify the effect of anisotropy on reaction rate (even before any dissolution), we calculate separately the contribution to the reaction rates from longitudinal and transverse channels, Ω_{x0} and Ω_{y0}, using $\Omega_I = (1/\Sigma_I s)\,\Sigma_I(s\Omega)$ where the summation is performed over all the longitudinal ($I = x$) or transverse channels ($I = y$) at $t = 0$.

Calculation of the initial reaction rate, Ω_{S0}, in the network shows that when the reaction is transport controlled (large G), it varies by an order of magnitude, depending on the anisotropy degree (black solid line in Figure 7a). The reaction rate is low for negative χ, due to significant diffusive inhibition of the dissolution in transverse channels, Ω_{y0}, and increases with increasing χ (red line). In contrast, the reaction rate in longitudinal channels, Ω_{x0}, is almost independent of χ (blue line). Although Ω_{y0} increases dramatically for large χ, it is only partially reflected in the bulk reaction rate Ω_{S0}, due to the low surface area of the longitudinal channels compared to the transverse ones. Following dissolution, as the channels widen, the bulk rate, Ω_{St}, decreases due to the diffusive limitation (see the dashed black line in Figure 7a which shows Ω_{St} at the time when $k/k_0 = 10^3$). Intermediate conditions ($G = 1$) show a similar trend as the fully transport-controlled regime but with weaker effects (Figure 7b).

In contrast, under surface-controlled reaction conditions (low G), the reaction rate is nearly independent of anisotropy degree and also does not change appreciably following dissolution (Figure 7c). Slightly slower reaction rates are observed for low χ, due to the large surface area of the transverse channels, leading to increased dissolved concentration which reduces the driving force for reaction.

4. Applicability to Field Conditions

Lastly, we discuss the relevance of the results presented here to geological systems. In particular, we characterize the conditions for which geological media are subjected to similar reactive flow conditions and alterations as the ones studied here (Figure 8). The large variability in mineralogy characteristics of geological media results in a large range of reaction rates, Ω_S, and kinetic coefficients, λ. Examples for common rapid reactions ($\lambda \sim 10^{-4}$ m/s) include limestone dissolution by acidic solutions (pH $\sim$ 3; Peng et al., 2015; Plummer et al., 1978) or of halite by water (Alkattan et al., 1997). Intermediate rates occur in gypsum ($\lambda \sim 10^{-6}$ m/s; Colombani, 2008) and limestone karst (pH $\sim$ 6, $\lambda \sim 10^{-7}$ m/s; Dreybrodt et al., 2005; Palmer, 1991), in all of which dissolution is commonly described using first-order kinetics (except close to saturation). Slower
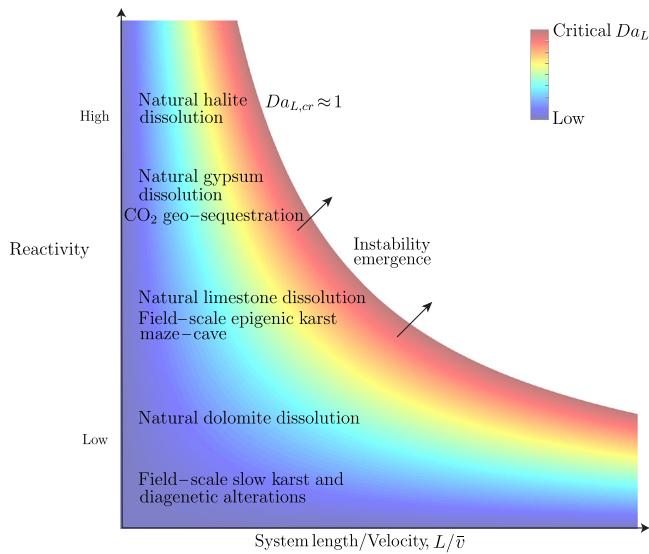
Figure 8. Uniform dissolution in different geological systems takes place when Da_L (Equation 18) is lower than the critical Damköhler number $Da_{L,cr} \approx 1$ (colored region). When $Da_{L,cr} > 1$, the wormholing instability emerges (Starchenko & Ladd, 2018). Under lower reactivity, uniform dissolution is expected to take place over larger length scales, L, and under lower fluid velocities, u. Reactivity is the product of λ^{eff} and the specific surface area, S, assumed constant here.

reaction is observed when dolomite lithology is involved (Busenberg & Plummer, 1982; Morse & Arvidson, 2002) or if the groundwater composition is close to saturation, where higher-order kinetics is observed (Dreybrodt et al., 2005; Palmer, 2011). An even slower dissolution reaction occurs in feldspar minerals (Li et al., 2006; Zhu, 2005).

This large variability in reaction rates suggests that low Da_L conditions and uniform dissolution can persist under a wide range of flow conditions or length scales (Steefel & Lasaga, 1990). However, for highly reactive systems a field-scale uniform dissolution can only take place under relatively high flow rates. For example, let us consider a range of system reactivities, $\lambda = 10^{-4}, 10^{-7}$, and 10^{-10} m/s, with a characteristic length scale, L, of 0.1 km and of specific surface areas, $S = 0.1$ m^{-1} for fractured media (Pacheco & Alencoão, 2006; Pacheco & Van der Weijden, 2014) to 10^4 m^{-1} for porous rocks (Mostaghimi et al., 2013; Noiriel et al., 2012). A relatively uniform dissolution, characterized by $Da_L = 0.1$ (Equation 18), requires Darcy flux of $\overline{v} > 10^{-2}$ m/s for highly reactive systems ($\lambda \sim 10^{-4}$ m/s), $\overline{v} > 10^{-5}$ m/s for moderate reactivity ($\lambda \sim 10^{-7}$ m/s), and $\overline{v} > 10^{-8}$ m/s for $\lambda \approx 10^{-10}$ m/s. High fluxes can occur in permeable shallow aquifers, especially in fractured (Kolditz, 2001; Palmer, 1991) and karstic media (Ford & Williams, 2013; White, 2002) and near pumping wells (Bear & Cheng, 2010; Niemi et al., 2017). However, in most cases, the flow rates are not high enough for uniform alterations to take place in highly reactive systems (Szymczak & Ladd, 2012) unless the system size is relatively small (~cm; Golfier et al., 2002; Menke et al., 2017). Consequently, nonuniform dissolution patterns (channeling) are typically observed in fast-reacting systems at the field scale (Bosák et al., 2016; Frumkin, 1994). In fact, even for high rate CO_2 injections involving high reactivity, uniform dissolution is only expected at a large distance from the injection well, after pH sufficiently increases and reactivity drops (Luquot & Gouze, 2009; Niemi et al., 2017).

There is however evidence that field-scale uniform dissolution in carbonates can take place under natural conditions (moderate reactivity). Some karstic maze-like caves are formed by rapid floodwater flow into the entire fracture network, which leads to their uniform enlargement into an extensive network of passages, over time scales of 10^4–10^5 years (Howard & Groves, 1995; Palmer, 1991, 2011). Exceptionally, a similar phenomenon is even documented to take place in highly reactive salt rock (Frumkin, 2013). It is noted that modeling of developed speleogenesis and large passage formation is beyond the scope of this work. Yet maze-cave formation is a good example of homogeneous dissolution at the system scale, which is limited by reaction, compatible with the uniformly dissolved systems analyzed in the present study.

Furthermore, carbonate dissolution can be remarkably slow, if induced by groundwater with a composition close to calcium saturation, producing significant karst and large speleological structures over time scales of millions of years (Dreybrodt et al., 2005; Frumkin et al., 2017; Palmer, 2011). In field-scale systems ($L > 0.1$ km) with groundwater close to saturation, a uniform dissolution may control karst evolution in fractured media even under the low groundwater velocities expected in deep aquifers (>1 km), where Darcy flux may be of the order of ~10^{-7} m/s (Garven, 1995; Gvirtzman et al., 1997), or under higher flow rates in porous rocks where specific surface area, S, is large (Mostaghimi et al., 2013; Noiriel et al., 2012).

As for the reaction regime (characterized by the transport parameter G), we note that the reaction can be transport controlled if the reaction rate coefficient, λ, is high or if the pore sizes or apertures are large, leading to inhibition of reaction by diffusive transport that becomes substantial for $G > $ ~0.1. For example, considering $G = 0.1$ (Equation 19), $Sh = 4$, $D \approx 10^{-9}$ m^2/s, and initial pore size of $r \sim 10^{-5}$–10^{-3} m (Blunt, 2017; Dreybrodt et al., 2005; Peng et al., 2015) provides $\lambda \sim 10^{-7}$–10^{-5} m/s. This implies that relatively fast geochemical systems, as well as limestone karstic systems, can be within the transport-controlled reaction regime.

5. Summary and Conclusions

We have studied uniform dissolution in heterogeneous and anisotropic media using a 2-D network model. In this regime, dissolution takes place throughout the medium, leading to a homogenization of the medium and consequently of the flow field, which is expected to be even more pronounced in 3-D networks. When transverse channels are wide compared to longitudinal ones, the flow field is initially highly heterogeneous and the flow is focused in a few tortuous pathways. In such media, the dissolution-induced homogenization effect is very pronounced and the preferential tortuous flow paths are eliminated quickly. Furthermore, uniform dissolution always leads to a reduction in anisotropy, even when the injection is in the direction of the wider, more conductive channels. In the transport-controlled regime, the homogenization is further enhanced because the diffusive hindrance is weaker in the narrow channels and leads to their selective enlargement.

The initial anisotropy degree also controls the permeability evolution: For wide transverse channels and heterogeneous flow field, initial permeability is high and its enhancement by dissolution is relatively slow. In the opposite case of narrow transverse channels, the ability of the flow to bypass narrow constrictions is limited; therefore, the initial permeability is low and its enhancement is much more rapid. At the uniform regime, the underlying mechanism for permeability enhancement is the enlargement of the less conductive channels. This is in contrast to the wormholing regime at higher Da_L, where preferential pathways are enhanced (Golfier et al., 2002; Szymczak & Ladd, 2009). The reaction regime, characterized by the transport parameter G, has an intricate effect on the permeability evolution: This has been demonstrated for an idealized model medium of a channel with a wavy profile. For transport-controlled dissolution (large G), permeability initially increases rapidly due to selective dissolution of the narrower constrictions, whereas at later stages transport inhibition gains importance and permeability enhancement becomes slower compared to surface-controlled reaction conditions.

Further, it is shown that the pore-scale reaction regime and anisotropy degree control the macroscopic reaction rates, which depend on the intrinsic kinetic rate and the transport conditions. At a transport-controlled regime, bulk reaction rates change by almost an order of magnitude depending on initial anisotropy degree and following dissolution and widening of the channels, whereas in the surface-controlled regime bulk reaction rates barely change. Finally, we discuss the relevance of the results presented here to geological systems and characterize the conditions for which geological media are subjected to uniform alterations. We also discuss field-scale examples of karstic homogeneous dissolution.

Our findings show that within the uniform dissolution regime the medium becomes more homogenous and isotropic, in contrast to the higher Da_L regime when heterogeneity increases with the dissolution and wormholes develop (Aharonov et al., 1997; Upadhyay et al., 2015). The results provide insights into the link between void-space geometry and the evolution of macroscopic properties of geological media due to the dissolution. These findings contribute to our understanding of geological processes such as diagenesis or karst evolution in fractured media, as well as of engineering applications such as carbon geosequestration and groundwater management.

Appendix A: Dissolution in Wavy Channel

We consider dissolution in a cylindrical channel of length L, of initially wavy profile (black line in Figure 6a)

$$r(x, t = 0) = r_0 + U \sin(\omega x), \tag{A1}$$

where x is the axial coordinate and U and ω are amplitude and angular frequency. The derivation below is analogous to that in Budek and Szymczak (2012) but for the different initial conditions considered. Here, we assume low Reynolds number and small amplitude of the corrugations. Under these conditions the velocity profile can be assumed to be locally parabolic. At higher Reynolds number the flow separation takes place and vortices appear (Deiber & Schowalter, 1979; Esquivel et al., 2012) which affect mass transport (Dykaar & Kitanidis, 1996).

The channel erodes according to

$$\frac{\partial \hat{r}}{\partial t} = \frac{1}{r_0} \frac{\lambda \gamma}{1 + G\hat{r}} \hat{c},$$ (A2)

where $\gamma = c_{eq}/c_{sol}\nu$, $G = \lambda 2r_0/ShD$, $\hat{c} = (c_{eq}\text{-}c)/c_{eq}$, and the scaled radius is $\hat{r} = r/r_0$. With those definitions Equation 10 in the main text gives

$$\frac{\partial \hat{c}}{\partial x} = -\frac{2\pi r_0 \lambda}{q} \frac{\hat{r}}{1 + G\hat{r}} \hat{c}.$$ (A3)

Introducing the scaled time $\hat{t} = \lambda\gamma t/r_0$ and axial coordinate $\hat{x} = x/L$, Equation A2 becomes

$$\frac{\partial \hat{r}}{\partial \hat{t}} = \frac{1}{1 + G\hat{r}} \hat{c},$$ (A4)

whereas Equation A3 takes the form

$$\frac{\partial \hat{c}}{\partial \hat{x}} = -\frac{2\pi r_0 L\lambda}{q} \frac{\hat{r}}{1 + G\hat{r}} \hat{c} = -(1 + G)Da_W \frac{\hat{r}}{1 + G\hat{r}} \hat{c},$$ (A5)

where the channel Damköhler number is

$$Da_W = \frac{2\pi r_0 L\lambda/q}{1 + G}.$$ (A6)

Differentiating Equation A4 with respect to $\hat{x}$ and using Equation A5 leads to

$$\frac{\partial}{\partial \hat{x}} \frac{\partial \hat{r}}{\partial \hat{t}} = -(1 + G)Da_W \frac{\hat{r}}{(1 + G\hat{r})^2} \hat{c} - \frac{G}{(1 + G\hat{r})^2} \hat{c} \frac{\partial \hat{r}}{\partial \hat{x}}.$$ (A7)

Further, expressing $\hat{c}$ through the derivative $\partial\hat{r}/\partial\hat{t}$ using Equation A4 provides equation in terms of $\hat{r}$ alone,

$$\frac{\partial}{\partial \hat{x}} \frac{\partial \hat{r}}{\partial \hat{t}} = -(1 + G)Da_W \frac{\hat{r}}{1 + G\hat{r}} \frac{\partial \hat{r}}{\partial \hat{t}} - \frac{G}{1 + G\hat{r}} \frac{\partial \hat{r}}{\partial \hat{t}} \frac{\partial \hat{r}}{\partial \hat{x}}.$$ (A8)

Next, integrating over time gives

$$\frac{\partial}{\partial \hat{x}} \left[\hat{r} \left(1 + G\frac{\hat{r}}{2} \right) \right] + \frac{1}{2}(1 + G)Da_W \hat{r}^2 = W(\hat{x}).$$ (A9)

The function $W(\hat{x})$ can be solved using the initial condition of the scaled Equation A1

$$\hat{r}(\hat{x}, \hat{t} = 0) = 1 + \hat{U}\sin(\hat{\omega}\hat{x}).$$ (A10)

This provides

$$W(\hat{x}) = \hat{\omega}\hat{U}\cos(\hat{\omega}\hat{x})(1 + G\hat{r}_{t_0}) + \frac{1}{2}(1 + G)Da_W \hat{r}_{t_0}^2,$$ (A11)

where $\hat{r}_{t_0} = \hat{r}(x, t = 0)$. Substituting it back leads to the ODE

$$\frac{\partial \hat{r}}{\partial \hat{x}} = \frac{\hat{\omega}\hat{U}\cos(\hat{\omega}\hat{x})(1 + G\hat{r}_{t_0}) + \frac{1}{2}(1 + G)Da_W \left(\hat{r}_{t_0}^2 - \hat{r}^2 \right)}{1 + G\hat{r}},$$ (A12)

which can be solved numerically with the boundary condition $\hat{r}(\hat{x} = 0, \hat{t}) = \hat{r}_{in}(\hat{t})$, attained by solving Equation A4 with $\hat{c} = 1$

$$\frac{\partial \hat{r}_{in}}{\partial \hat{t}} = \frac{1}{1 + G\hat{r}_{in}}, \tag{A13}$$

resulting in

$$\hat{r}_{in}(\hat{t}) = \frac{\sqrt{2G\hat{t} + G(G+2) + 1} - 1}{G}. \tag{A14}$$

For the case of a fully transport-controlled reaction, $G \to \infty$, Equation A12 reduces to

$$\frac{\partial \hat{r}^2}{\partial \hat{x}} = 2\hat{r}_{t_0}\,\hat{\omega}\,\hat{U}\cos(\hat{\omega}\,\hat{x}) + Da_W\left(\hat{r}_{t_0}^2 - \hat{r}^2\right), \tag{A15}$$

which has the analytical solution

$$\begin{aligned}
\hat{r} = \Bigg[e^{-Da_W\hat{x}}\Bigg(\frac{2Da_W\hat{U}(\hat{\omega}-1)}{Da_W^2 + \hat{\omega}^2} - \frac{2\hat{U}^2(\hat{\omega}-1)\hat{\omega}}{Da_W^2 + 4\hat{\omega}^2} + \frac{2\hat{t}}{G} \Bigg) + \frac{1}{2}\Big(2 + \hat{U}^2 \\
+ \hat{U}\Bigg(\frac{4Da_W(\hat{\omega}-1)\cos(\hat{\omega}\,\hat{x})}{Da_W^2 + \hat{\omega}^2} - \frac{\hat{U}\left(Da_W^2 + 4\hat{\omega}\right)\cos(2\hat{\omega}\,\hat{x})}{Da_w^2 + 4\hat{\omega}^2} + \frac{4\left(Da_W^2 + \hat{\omega}\right)\sin(\hat{\omega}\,\hat{x})}{Da_W^2 + \hat{\omega}^2} \\
- \frac{2Da_W\hat{U}(\hat{\omega}-1)\sin(2\hat{\omega}\,\hat{x})}{Da_W^2 + 4\hat{\omega}^2} \Bigg) \Bigg) \Bigg]^{\frac{1}{2}}.
\end{aligned} \tag{A16}$$

Appendix B: Permeability of a Channel of Variable Cross Section

Assuming that the flow profile at each cross section along the channel is parabolic, Hagen-Poiseuille equation in a differential form can be written as follows:

$$q = \frac{\pi r^4}{8\mu}\frac{dp}{dx}. \tag{B1}$$

Integrating Equation B1 over the channel length, and dividing by the average channel cross section $a = \pi r_0^2$, leads to

$$\bar{u} = \frac{L}{8\mu r_0^2 \int_0^L \frac{dx}{r^4}}\frac{\Delta p}{L}, \tag{B2}$$

and the channel permeability is

$$k = \frac{L}{8\mu r_0^2 \int_0^L \frac{dx}{r^4}} \tag{B3}$$

which can be calculated by numerical integration over the channel profile attained by solving Equation A12 or A16.

Data Availability Statement

Data produced in this study are available online (https://doi.org/10.5281/zenodo.3988934).

References

Adler, P. M., Thovert, J.-F., & Mourzenko, V. V. (2013). *Fractured porous media*. Oxford, UK: Oxford University Press.

Agar, S. M., & Geiger, S. (2015). Fundamental controls on fluid flow in carbonates: Current workflows to emerging technologies. *Geological Society, London, Special Publications*, *406*(1), 1–59. https://doi.org/10.1144/SP406.18

Aharonov, E., Spiegelman, M., & Kelemen, P. (1997). Three-dimensional flow and reaction in porous media: Implications for the Earth's mantle and sedimentary basins. *Journal of Geophysical Research*, *102*(B7), 14,821–14,833.

Aharonov, E., Whitehead, J. A., Kelemen, P. B., & Spiegelman, M. (1995). Channeling instability of upwelling melt in the mantle. *Journal of Geophysical Research*, *100*(B10), 20433.

Algive, L., Bekri, S., Vizika, O., & others. (2010). Pore-network modeling dedicated to the determination of the petrophysical-property changes in the presence of reactive fluid. *SPE Journal*, *15*(03), 618–633. https://doi.org/10.2118/124305-PA

Alkattan, M., Oelkers, E. H., Dandurand, J.-L., & Schott, J. (1997). Experimental studies of halite dissolution kinetics, 1. The effect of saturation state and the presence of trace metals. *Chemical Geology*, *137*(3–4), 201–219. https://doi.org/10.1016/S0009-2541(96)00164-7

Ameli, P., Elkhoury, J. E., Morris, J. P., & Detwiler, R. L. (2014). Fracture permeability alteration due to chemical and mechanical processes: {A} coupled high-resolution model. *Rock Mechanics and Rock Engineering*, *47*(5), 1563–1573. https://doi.org/10.1007/s00603-014-0575-z

Audra, P., & Palmer, A. N. (2015). Research frontiers in speleogenesis. Dominant processes, hydrogeological conditions and resulting cave patterns. *Acta Carsologica*, *44*(3), 315–348.

Aydan, Ö., Shimizu, Y., & Kawamoto, T. (1996). The anisotropy of surface morphology characteristics of rock discontinuities. *Rock Mechanics and Rock Engineering*, *29*(1), 47–59. https://doi.org/10.1007/BF01019939

Baas, J. H., Hailwood, E. A., McCaffrey, W. D., Kay, M., & Jones, R. (2007). Directional petrological characterisation of deep-marine sandstones using grain fabric and permeability anisotropy: Methodologies, theory, application and suggestions for integration. *Earth-Science Reviews*, *82*(1–2), 101–142. https://doi.org/10.1016/j.earscirev.2007.02.003

Barton, N. (2006). *Rock quality, seismic velocity, attenuation and anisotropy*. London, UK: CRC Press.

Bear, J., & Cheng, A. H.-D. (2010). *Modeling groundwater flow and contaminant transport* (Vol. 23). Dordrecht, Netherlands: Springer Science & Business Media.

Bejan, A. (2013). *Convection heat transfer*. Hoboken, NJ: John Wiley & Sons.

Bekri, S., Thovert, J. F., & Adler, P. M. (1995). Dissolution of porous media. *Chemical Engineering Science*, *50*(17), 2765–2791. https://doi.org/10.1016/0009-2509(95)00121-K

Bense, V. F., Gleeson, T., Loveless, S. E., Bour, O., & Scibek, J. (2013). Fault zone hydrogeology. *Earth-Science Reviews*, *127*, 171–192. https://doi.org/10.1016/j.earscirev.2013.09.008

Benson, P. M., Meredith, P. G., Platzman, E. S., & White, R. E. (2005). Pore fabric shape anisotropy in porous sandstones and its relation to elastic wave velocity and permeability anisotropy under hydrostatic pressure. *International Journal of Rock Mechanics and Mining Sciences*, *42*(7–8), 890–899. https://doi.org/10.1016/j.ijrmms.2005.05.003

Bijeljic, B., & Blunt, M. J. (2006). Pore-scale modeling and continuous time random walk analysis of dispersion in porous media. *Water Resources Research*, *42*, W01202. https://doi.org/10.1029/2005WR004578

Blenkinsop, T. G., Oliver, N., & Cihan, M. (2007). Quantifying fabric anisotropy in breccias: Insights into brecciation in a mineralizing environment. *American Geophysical Union, Fall Meeting 2007, abstract id. MR21A-05*.

Blunt, M. J. (2017). *Multiphase flow in permeable media: A pore-scale perspective*. Cambridge, UK: Cambridge University Press.

Bonnet, E., Bour, O., Odling, N. E., Davy, P., Main, I., Cowie, P., & Berkowitz, B. (2001). Scaling of fracture systems in geological media. *Reviews of Geophysics*, *39*(3), 347–383.

Bosák, P., Bruthans, J., Filippi, M., Svoboda, T., & Šmíd, J. (2016). Karst and caves in salt diapirs, SE Zagros Mts.(Iran). *Acta Carsologica*, *28*(2), 41–75. https://doi.org/10.3986/ac.v28i2.484

Boutt, D. F., Cook, B. K., McPherson, B. J. O. L., & Williams, J. R. (2007). Direct simulation of fluid-solid mechanics in porous media using the discrete element and lattice-Boltzmann methods. *Journal of Geophysical Research*, *112*, 1–13, https://doi.org/10.1029/2004JB003213

Brown, S. R., & Scholz, C. H. (1985). Broad bandwidth study of the topography of natural rock surfaces. *Journal of Geophysical Research*, *90*(B14), 12,575–12,582.

Bruno, M. S. (1994). Micromechanics of stress-induced permeability anisotropy and damage in sedimentary rock. *Mechanics of Materials*, *18*(1), 31–48. https://doi.org/10.1016/0167-6636(94)90004-3

Budek, A., & Szymczak, P. (2012). Network models of dissolution of porous media. *Physical Review E*, *86*(5), 056318. https://doi.org/10.1103/PhysRevE.86.056318

Busenberg, E., & Plummer, L. N. (1982). The kinetics of dissolution of dolomite in CO2-H2O systems at 1.5 to 65°C and 0 to 1 atm PCO2. *American Journal of Science*, *282*(1), 45–78.

Candela, T., Renard, F., Klinger, Y., Mair, K., Schmittbuhl, J., & Brodsky, E. E. (2012). Roughness of fault surfaces over nine decades of length scales. *Journal of Geophysical Research*, *117*, B08409 https://doi.org/10.1029/2011JB009041

Clavaud, J.-B., Maineult, A., Zamora, M., Rasolofosaon, P., & Schlitter, C. (2008). Permeability anisotropy and its relations with porous medium structure. *Journal of Geophysical Research*, *113*, B01202. https://doi.org/10.1029/2007JB005004

Colombani, J. (2008). Measurement of the pure dissolution rate constant of a mineral in water. *Geochimica et Cosmochimica Acta*, *72*(23), 5634–5640.

Daccord, G., & Lenormand, R. (1987). Fractal patterns from chemical dissolution. *Nature*, *325*, 41–43. https://doi.org/10.1038/325041a0

Daccord, G., Lietard, O., & Lenormand, R. (1993). Chemical dissolution of a porous medium by a reactive fluid—II. Convection vs reaction, behavior diagram. *Chemical Engineering Science*, *48*(1), 179–186. https://doi.org/10.1016/0009-2509(93)80294-Z

De Boever, E., Varloteaux, C., Nader, F. H., Foubert, A., Békri, S., Youssef, S., & Rosenberg, E. (2012). Quantification and prediction of the 3D pore network evolution in carbonate reservoir rocks. *Oil & Gas Science and Technology–Revue d'IFP Energies Nouvelles*, *67*(1), 161–178.

Deiber, J. A., & Schowalter, W. R. (1979). Flow through tubes with sinusoidal axial variations in diameter. *AICHE Journal*, *25*(4), 638–645.

Deng, H., Molins, S., Trebotich, D., Steefel, C., & DePaolo, D. (2018). Pore-scale numerical investigation of the impacts of surface roughness: Upscaling of reaction rates in rough fractures. *Geochimica et Cosmochimica Acta*, *239*, 374–389.

Deng, H., Steefel, C. I., Molins, S., & DePaolo, D. (2018). Fracture evolution in multimineral systems: The role of mineral composition, flow rate, and fracture aperture heterogeneity. *ACS Earth and Space Chemistry*, *2*(2), 112–124. https://doi.org/10.1021/acsearthspacechem.7b00130

Detwiler, R. L., & Rajaram, H. (2007). Predicting dissolution patterns in variable aperture fractures: Evaluation of an enhanced depth-averaged computational model. *Water Resources Research*, *43*, W04403. https://doi.org/10.1029/2006WR005147

Dove, P. M., & Crerar, D. A. (1990). Kinetics of quartz dissolution in electrolyte solutions using a hydrothermal mixed flow reactor. *Geochimica et Cosmochimica Acta*, *54*(4), 955–969.

Dreybrodt, W. (1988). *Processes in karst systems, physics, chemistry, and geology*. Berlin, Heidelberg: Springer.

Dreybrodt, W., Gabrovšek, F., & Romanov, D. (2005). *Processes of a speleogenessis [sic]: A modeling approach* (Vol. 4). Ljubljana, Slovenia: Založba ZRC.

Dykaar, B. B., & Kitanidis, P. K. (1996). Macrotransport of a biologically reacting solute through porous media. *Water Resources Research*, *32*(2), 307–320.

Esquivel, P. I. R., Boonkkamp, J. H. M., & Dam, J. A. M. (2012). An asymptotic formula for the friction factor of laminar flow in pipes of varying cross section. *Mathematics in Engineering, Science & Aerospace (MESA)*, *3*(1), 63–78.

Filipponi, M., Jeannin, P.-Y., & Tacher, L. (2009). Evidence of inception horizons in karst conduit networks. *Geomorphology*, *106*(1–2), 86–99. https://doi.org/10.1016/j.geomorph.2008.09.010

Fiori, A., & Jankovic, I. (2012). On preferential flow, channeling and connectivity in heterogeneous porous formations. *Mathematical Geosciences*, *44*(2), 133–145.

Ford, D., & Williams, P. D. (2013). *Karst hydrogeology and geomorphology*. Chichester, UK: John Wiley & Sons.

Fredd, C. N., & Fogler, H. S. (1998). Influence of transport and reaction on wormhole formation in porous media. *AICHE Journal*, *44*(9), 1933–1949.

Friedman, S. P., & Jones, S. B. (2001). Measurement and approximate critical path analysis of the pore-scale-induced anisotropy factor of an unsaturated porous medium. *Water Resources Research*, *37*(12), 2929–2942.

Frumkin, A. (1994). Morphology and development of salt caves. *National Speleological Society Bulletin*, *56*, 82–95.

Frumkin, A. (2013). *Salt karst [in:] Treatise on geomorphology. Vol. 6: Karst geomorphology*. San Diego, CA: Academic Press.

Frumkin, A., Langford, B., Lisker, S., & Amrani, A. (2017). Hypogenic karst at the Arabian platform margins: Implications for far-field groundwater systems. *GSA Bulletin*, *129*(11–12), 1636–1659. https://doi.org/10.1130/B31694.1

Garven, G. (1995). Continental-scale groundwater flow and geologic processes. *Annual Review of Earth and Planetary Sciences*, *23*(1), 89–117.

Golfier, F., Zarcone, C., Bazin, B., Lenormand, R., Lasseux, D., & Quintard, M. (2002). On the ability of a Darcy-scale model to capture wormhole formation during the dissolution of a porous medium. *Journal of Fluid Mechanics*, *457*, 213–254. https://doi.org/10.1017/S0022112002007735

Gouze, P., Noiriel, C., Bruderer, C., Loggia, D., & Leprovost, R. (2003). X-ray tomography characterization of fracture surfaces during dissolution. *Geophysical Research Letters*, *30*(5).

Gueguen, Y., & Schubnel, A. (2003). Elastic wave velocities and permeability of cracked rocks. *Tectonophysics*, *370*(1–4), 163–176. https://doi.org/10.1016/S0040-1951(03)00184-7

Gupta, N., & Balakotaiah, V. (2001). Heat and mass transfer coefficients in catalytic monoliths. *Chemical Engineering Science*, *56*(16), 4771–4786. https://doi.org/10.1016/S0009-2509(01)00134-8

Gvirtzman, H., Garven, G., & Gvirtzman, G. (1997). Thermal anomalies associated with forced and free ground-water convection in the Dead Sea rift valley. *Geological Society of America Bulletin*, *109*(9), 1167–1176. https://doi.org/10.1130/0016-7606(1997)109<1167: TAAWFA>2.3.CO;2

Hanna, R. B., & Rajaram, H. (1998). Influence of aperture variability on dissolutional growth of fissures in karst formations. *Water Resources Research*, *34*(11), 2843–2853.

Hayes, R. E., & Kolaczkowski, S. T. (1994). Mass and heat transfer effects in catalytic monolith reactors. *Chemical Engineering Science*, *49*(21), 3587–3599.

Hoefner, M. L., & Fogler, H. S. (1988). Pore evolution and channel formation during flow and reaction in porous media. *AICHE Journal*, *34*(1), 45–54. https://doi.org/10.1002/aic.690340107

Howard, A. D., & Groves, C. G. (1995). Early development of karst systems: 2. Turbulent flow. *Water Resources Research*, *31*(1), 19–26.

Huenges, E., & Ledru, P. (2011). *Geothermal energy systems: Exploration, development, and utilization*. Weinheim, Germany: John Wiley & Sons.

Hunt, A., & Ewing, R. (2009). Specific examples of critical path analysis. In *Percolation theory for flow in porous media* (pp. 97–122). Heidelberg, Germany: Springer.

Jang, J., Narsilio, G. A., & Santamarina, J. C. (2011). Hydraulic conductivity in spatially varying media—A pore-scale investigation. *Geophysical Journal International*, *184*(3), 1167–1179. https://doi.org/10.1111/j.1365-246X.2010.04893.x

Kang, P. K., Lei, Q., Dentz, M., & Juanes, R. (2018). Stress-induced anomalous transport in natural fracture networks. *Water Resources Research*. *55*, 4163–4185. https://doi.org/10.1029/2019WR024944

Kaufmann, G., & Braun, J. (1999). Karst aquifer evolution in fractured rocks. *Water Resources Research*, *35*(11), 3223–3238.

Kelemen, P. B., Whitehead, J. A., Aharonov, E., & Jordahl, K. A. (1995). Experiments on flow focusing in soluble porous media, with applications to melt extraction from the mantle. *Journal of Geophysical Research*, *100*(B1), 475–496.

Klimchouk, A. (2017). Types and settings of hypogene karst. In *Hypogene karst regions and caves of the world* (pp. 1–39). New York: Springer.

Kolditz, O. (2001). Non-linear flow in fractured rock. *International Journal of Numerical Methods for Heat & Fluid Flow*, *11*(6), 547–575. https://doi.org/10.1108/EUM0000000005668

Koponen, A., Kataja, M., & Timonen, J. (1996). Tortuous flow in porous media. *Physical Review E*, *54*(1), 406. https://doi.org/10.1103/PhysRevE.54.406

Ladd, A. J. C., & Szymczak, P. (2017). Use and misuse of large-density asymptotics in the reaction-infiltration instability. *Water Resources Research*, *53*, 2419–2430. https://doi.org/10.1002/2016WR019263

Lee, J.-J., & Bruhn, R. L. (1996). Structural anisotropy of normal fault surfaces. *Journal of Structural Geology*, *18*(8), 1043–1059. https://doi.org/10.1016/0191-8141(96)00022-3

Li, L., Peters, C. A., & Celia, M. A. (2006). Upscaling geochemical reaction rates using pore-scale network modeling. *Advances in Water Resources*, *29*, 1351–1370. https://doi.org/10.1016/j.advwatres.2005.10.011

Li, L., Peters, C. A., & Celia, M. A. (2007). Applicability of averaged concentrations in determining geochemical reaction rates in heterogeneous porous media. *American Journal of Science*, *307*(10), 1146–1166.

Li, L., Steefel, C. I., & Yang, L. (2008). Scale dependence of mineral dissolution rates within single pores and fractures. *Geochimica et Cosmochimica Acta*, *72*(2), 360–377. https://doi.org/10.1016/j.gca.2007.10.027

Lichtner, P. C. (1991). The quasi-stationary state approximation to fluid/rock reaction: Local equilibrium revisited. In J. Ganguly (Ed.), *Diffusion, atomic ordering, and mass transport: Selected topics in geochemistry* (pp. 452–560). New York, NY: Springer US.

Lichtner, P. C., Steefel, C. I., & Oelkers, E. H. (2018). *Reactive transport in porous media* (Vol. 34). Berlin, Germany: Walter de Gruyter GmbH & Co KG.

Liu, M., & Mostaghimi, P. (2017). Pore-scale simulation of dissolution-induced variations in rock mechanical properties. *International Journal of Heat and Mass*, *111*, 842–851. https://doi.org/10.1016/j.ijheatmasstransfer.2017.04.049

Lucia, F. J. (2007). *Carbonate reservoir characterization: An integrated approach* (2nd ed.). Berlin Heidelberg: Springer-Verlag.

Luquot, L., & Gouze, P. (2009). Experimental determination of porosity and permeability changes induced by injection of CO_2 into carbonate rocks. *Chemical Geology*, *265*(1–2), 148–159. https://doi.org/10.1016/j.chemgeo.2009.03.028

MATLAB, V (2018). *9.4. 0 (R2018a). The MathWorks Inc*. Natick, MA: USA.

Matyka, M., & Koza, Z. (2012). How to calculate tortuosity easily? *AIP Conference Proceedings*, *1453*, 17–22. https://doi.org/10.1063/1.4711147

Menke, H. P., Bijeljic, B., & Blunt, M. J. (2017). Dynamic reservoir-condition microtomography of reactive transport in complex carbonates: Effect of initial pore structure and initial brine pH. *Geochimica et Cosmochimica Acta*, *204*, 267–285. https://doi.org/10.1016/j.gca.2017.01.053

Min, K.-B., Rutqvist, J., Tsang, C.-F., & Jing, L. (2004). Stress-dependent permeability of fractured rock masses: A numerical study. *International Journal of Rock Mechanics and Mining Sciences*, *41*(7), 1191–1210. https://doi.org/10.1016/j.ijrmms.2004.05.005

Mitchell, T. M., & Faulkner, D. R. (2008). Experimental measurements of permeability evolution during triaxial compression of initially intact crystalline rocks and implications for fluid flow in fault zones. *Journal of Geophysical Research*, *113*, B11412. https://doi.org/10.1029/2008JB005588

Molins, S. (2015). Reactive interfaces in direct numerical simulation of pore-scale processes. *Reviews in Mineralogy and Geochemistry*, *80*, 461–481. https://doi.org/10.2138/rmg.2015.80.14

Morse, J. W., & Arvidson, R. S. (2002). The dissolution kinetics of major sedimentary carbonate minerals. *Earth-Science Reviews*, *58*(1–2), 51–84. https://doi.org/10.1016/S0012-8252(01)00083-6

Mostaghimi, P., Blunt, M. J., & Bijeljic, B. (2013). Computations of absolute permeability on micro-CT images. *Mathematical Geosciences*, *45*(1), 103–125. https://doi.org/10.1007/s11004-012-9431-4

Niemi, A., Bear, J., & Bensabat, J. (2017). *Geological storage of CO_2 in deep saline formations*. Dordrecht, Netherlands: Springer.

Nogues, J. P., Fitts, J. P., Celia, M. A., & Peters, C. A. (2013). Permeability evolution due to dissolution and precipitation of carbonates using reactive transport modeling in pore networks. *Water Resources Research*, *49*, 6006–6021. https://doi.org/10.1002/wrcr.20486

Noiriel, C., & Deng, H. (2018). Evolution of planar fractures in limestone: The role of flow rate, mineral heterogeneity and local transport processes. *Chemical Geology*, *497*, 100–114.

Noiriel, C., Steefel, C. I., Yang, L., & Ajo-Franklin, J. (2012). Upscaling calcium carbonate precipitation rates from pore to continuum scale. *Chemical Geology*, *318–319*, 60–74. https://doi.org/10.1016/j.chemgeo.2012.05.014

Nordbotten, J. M., & Celia, M. A. (2011). *Geological storage of CO_2: Modeling approaches for large-scale simulation*. Hoboken, NJ: John Wiley & Sons.

Orr, F. M. (2009). Onshore geologic storage of CO_2. *Science*, *325*(5948), 1656–1658. https://doi.org/10.1126/science.1175677

Pacheco, F. A. L., & Alencão, A. M. P. (2006). Role of fractures in weathering of solid rocks: Narrowing the gap between laboratory and field weathering rates. *Journal of Hydrology*, *316*(1–4), 248–265. https://doi.org/10.1016/j.jhydrol.2005.05.003

Pacheco, F. A. L., & Van der Weijden, C. H. (2014). Role of hydraulic diffusivity in the decrease of weathering rates over time. *Journal of Hydrology*, *512*, 87–106. https://doi.org/10.1016/j.jhydrol.2014.02.041

Palmer, A. N. (1991). Origin and morphology of limestone caves. *Geological Society of America Bulletin*, *103*(1), 1–21. https://doi.org/10.1130/0016-7606(1991)103<0001:OAMOLC>2.3.CO;2

Palmer, A. N. (2011). Distinction between epigenic and hypogenic maze caves. *Geomorphology*, *134*(1–2), 9–22. https://doi.org/10.1016/j.geomorph.2011.03.014

Peng, C., Crawshaw, J. P., Maitland, G. C., & Trusler, J. P. M. (2015). Kinetics of calcite dissolution in CO_2-saturated water at temperatures between (323 and 373) K and pressures up to 13.8 MPa. *Chemical Geology*, *403*, 74–85. https://doi.org/10.1016/j.chemgeo.2015.03.012

Pereira Nunes, J. P., Bijeljic, B., & Blunt, M. J. (2016). Pore-space structure and average dissolution rates: A simulation study. *Water Resources Research*, *52*, 7198–7212. https://doi.org/10.1002/2016WR019313

Perne, M., Covington, M., & Gabrovsek, F. (2014). Evolution of karst conduit networks in transition from pressurized flow to free-surface flow. *Hydrology and Earth System Sciences*, *18*(11), 4617.

Pinder, G. F., & Celia, M. A. (2006). *Subsurface Hydrology*. https://doi.org/10.1002/0470044209

Plummer, L. N., Wigley, T. M. L., & Parkhurst, D. L. (1978). The kinetics of calcite dissolution in CO_2-water systems at 5 degrees to 60 degrees C and 0.0 to 1.0 atm CO_2. *American Journal of Science*, *278*(2), 179–216. https://doi.org/10.2475/ajs.278.2.179

Raoof, A., Nick, H. M., Wolterbeek, T. K. T., & Spiers, C. J. (2012). Pore-scale modeling of reactive transport in wellbore cement under CO_2 storage conditions. *International Journal of Greenhouse Gas Control*, *11*, S67–S77.

Rehrl, C., Birk, S., & Klimchouk, A. (2008). Conduit evolution in deep-seated settings: Conceptual and numerical models based on field observations. *Water Resources Research*, *44*, W11425. https://doi.org/10.1029/2008WR006905

Renard, F., Voisin, C., Marsan, D., & Schmittbuhl, J. (2006). High resolution 3D laser scanner measurements of a strike-slip fault quantify its morphological anisotropy at all scales. *Geophysical Research Letters*, *33*, L04305. https://doi.org/10.1029/2005GL025038

Roded, R., Paredes, X., & Holtzman, R. (2018). Reactive transport under stress: Permeability evolution in deformable porous media. *Earth and Planetary Science Letters*, *493*, 198–207. https://doi.org/10.1016/j.epsl.2018.04.041

Rohsenow, W. M., Hartnett, J. P., & Cho, Y. I. (1998). Handbook of heat transfer (Vol. 3). McGraw-Hill New York.

Sahimi, M. (2011). *Flow and transport in porous media and fractured rock: From classical methods to modern approaches*. Weinheim, Germany: John Wiley & Sons.

Sanford, W. E., & Konikow, L. F. (1989). Simulation of calcite dissolution and porosity changes in saltwater mixing zones in coastal aquifers. *Water Resources Research*, *25*(4), 655–667.

Sayers, C. M. (1990). Stress-induced fluid flow anisotropy in fractured rock. *Transport in Porous Media*, *5*(3), 287–297. https://doi.org/10.1007/BF00140017

Shafiq, M. U., & Mahmud, H. B. (2017). Sandstone matrix acidizing knowledge and future development. *Journal of Petroleum Exploration and Production Technology*, *7*(4), 1205–1216. https://doi.org/10.1007/s13202-017-0314-6

Simpson, G., Guéguen, Y., & Schneider, F. (2001). Permeability enhancement due to microcrack dilatancy in the damage regime. *Journal of Geophysical Research*, *106*(B3), 3999–4016.

Skoglund, R. Ø., Lauritzen, S.-E., & Gabrovšek, F. (2010). The impact of glacier ice-contact and subglacial hydrochemistry on evolution of maze caves: A modelling approach. *Journal of Hydrology*, *388*(1–2), 157–172. https://doi.org/10.1016/j.jhydrol.2010.04.037

Spiegelman, M., Kelemen, P. B., & Aharonov, E. (2001). Causes and consequences of flow organization during melt transport: The reaction infiltration instability in compactible media. *Journal of Geophysical Research*, *106*, 2061–2077.

Starchenko, V., & Ladd, A. J. C. (2018). The development of wormholes in laboratory-scale fractures: Perspectives from three-dimensional simulations. *Water Resources Research*, *54*, 7946–7959 https://doi.org/10.1029/2018WR022948

Steefel, C. I., & Lasaga, A. C. (1990). Evolution of dissolution patterns. In D. C. Melchior & R. L. Bassett (Eds.), *Chemical modeling of aqueous systems {II}* (pp. 212–225). Washington, DC: American Chemical Society.

Steefel, C. I., & Maher, K. (2009). Fluid-rock interaction: A reactive transport approach. *Reviews in Mineralogy and Geochemistry*, *70*(1988), 485–532. https://doi.org/10.2138/rmg.2009.70.11

Steefel, C. I., Molins, S., & Trebotich, D. (2013). Pore scale processes associated with subsurface CO2 injection and sequestration. *Reviews in Mineralogy and Geochemistry*, *77*(1), 259–303. https://doi.org/10.2138/rmg.2013.77.8

Szymczak, P., & Ladd, A. J. C. (2006). A network model of channel competition in fracture dissolution. *Geophysical Research Letters*, *33*, L05401. https://doi.org/10.1029/2005GL025334

Szymczak, P., & Ladd, A. J. C. (2009). Wormhole formation in dissolving fractures. *Journal of Geophysical Research*, *114*, B06203. https://doi.org/10.1029/2008JB006122

Szymczak, P., & Ladd, A. J. C. (2012). Reactive-infiltration instabilities in rocks. Fracture dissolution. *Journal of Fluid Mechanics*, *702*, 239–264.

Tansey, J., & Balhoff, M. T. (2016). Pore network modeling of reactive transport and dissolution in porous media. *Transport in Porous Media*, *113*(2), 303–327. https://doi.org/10.1017/jfm.2012.174

Tatone, B. S. A., & Grasselli, G. (2012). Quantitative measurements of fracture aperture and directional roughness from rock cores. *Rock Mechanics and Rock Engineering*, *45*(4), 619–629. https://doi.org/10.1007/s00603-011-0219-5

Taylor, T. R., Giles, M. R., Hathon, L. A., Diggs, T. N., Braunsdorf, N. R., Birbiglia, G. V, et al. (2010). Sandstone diagenesis and reservoir quality prediction: Models, myths, and reality. *AAPG Bulletin*, *94*(8), 1093–1132. https://doi.org/10.1306/04211009123

Thompson, M. E., & Brown, S. R. (1991). The effect of anisotropic surface roughness on flow and transport in fractures. *Journal of Geophysical Research*, *96*, 21,923–21,932.

Upadhyay, V. K., Szymczak, P., & Ladd, A. J. C. (2015). Initial conditions or emergence: What determines dissolution patterns in rough fractures? *Journal of Geophysical Research: Solid Earth*, *120*, 6102–6121. https://doi.org/10.1002/2015JB012233

Varloteaux, C., Vu, M. T., Békri, S., & Adler, P. M. (2013). Reactive transport in porous media: Pore-network model approach compared to pore-scale model. *Physical Review E*, *87*(2), 23010.

Wang, H., Bernabé, Y., Mok, U., & Evans, B. (2016). Localized reactive flow in carbonate rocks: Core-flood experiments and network simulations. *Journal of Geophysical Research: Solid Earth*, *121*, 7965–7983. https://doi.org/10.1002/2016JB013304

White, W. B. (2002). Karst hydrology: Recent developments and open questions. *Engineering Geology*, *65*(2–3), 85–105. https://doi.org/10.1016/S0013-7952(01)00116-8

Wray, R. A. L., & Sauro, F. (2017). An updated global review of solutional weathering processes and forms in quartz sandstones and quartzites. *Earth-Science Reviews*, *171*, 520–557. https://doi.org/10.1016/j.earscirev.2017.06.008

Wright, H. M. N., Cashman, K. V., Gottesfeld, E. H., & Roberts, J. J. (2009). Pore structure of volcanic clasts: Measurements of permeability and electrical conductivity. *Earth and Planetary Science Letters*, *280*(1–4), 93–104. https://doi.org/10.1016/j.epsl.2009.01.023

Xie, H., Wang, J.-A., & Kwaśniewski, M. A. (1999). Multifractal characterization of rock fracture surfaces. *International Journal of Rock Mechanics and Mining Sciences*, *36*(1), 19–27. https://doi.org/10.1016/S0148-9062(98)00172-7

Xiong, Q., Baychev, T. G., & Jivkov, A. P. (2016). Review of pore network modelling of porous media: Experimental characterisations, network constructions and applications to reactive transport. *Journal of Contaminant Hydrology*, *192*, 101–117. https://doi.org/10.1016/j.jconhyd.2016.07.002

Zhang, S., & DePaolo, D. J. (2017). Rates of CO2 mineralization in geological carbon storage. *Accounts of Chemical Research*, *50*(9), 2075–2084. https://doi.org/10.1021/acs.accounts.7b00334

Zhu, C. (2005). In situ feldspar dissolution rates in an aquifer. *Geochimica et Cosmochimica Acta*, *69*(6), 1435–1453. https://doi.org/10.1016/j.gca.2004.09.005